SISSA

PAPER • OPEN ACCESS

Selection of the silicon sensor thickness for the Phase-2 upgrade of the CMS Outer Tracker

View the article online for updates and enhancements.

Selection of the silicon sensor thickness for the Phase-2 upgrade of the CMS Outer Tracker

The Tracker group of the CMS collaboration

E-mail: alexander.dierlamm@kit.edu

ABSTRACT: During the operation of the CMS experiment at the High-Luminosity LHC the silicon sensors of the Phase-2 Outer Tracker will be exposed to radiation levels that could potentially deteriorate their performance. Previous studies had determined that planar float zone silicon with n-doped strips on a p-doped substrate was preferred over p-doped strips on an n-doped substrate. The last step in evaluating the optimal design for the mass production of about $200\,\mathrm{m}^2$ of silicon sensors was to compare sensors of baseline thickness (about $300\,\mathrm{\mu m}$) to thinned sensors (about $240\,\mathrm{\mu m}$), which promised several benefits at high radiation levels because of the higher electric fields at the same bias voltage. This study provides a direct comparison of these two thicknesses in terms of sensor characteristics as well as charge collection and hit efficiency for fluences up to $1.5 \times 10^{15}\,\mathrm{n_{eq}/cm^2}$. The measurement results demonstrate that sensors with about $300\,\mathrm{\mu m}$ thickness will ensure excellent tracking performance even at the highest considered fluence levels expected for the Phase-2 Outer Tracker.

Corresponding author: Alexander Dierlamm.

Contents

1 Introduction

The High-Luminosity LHC (HL-LHC [1, 2]) will provide an instantaneous luminosity of up to $(5–7.5) \times 10^{34}$ cm^{-2}s^{-1} during about ten years of operation. This will result in an unprecedented radiation environment and particle rate for the detectors at the HL-LHC. The CMS detector will be upgraded to cope with the new challenges (Phase-2 Upgrade). The new tracking system consists of an inner vertex detector with very high granularity and an outer tracking system comprising both strip and macro-pixel (1.4 mm short strips) sensors. The outer tracking system placed at a radial distance greater than 20 cm from the beam line of the CMS detector [3] will be exposed to a maximum fluence[1] of 1.05×10^{15} n$_{eq}$/cm^2 for an integrated luminosity of 3000 fb^{-1} or up to the ultimate fluence of 1.4×10^{15} n$_{eq}$/cm^2 after 4000 fb^{-1}. This is a much higher radiation level than the n-type silicon sensors in the current CMS tracker could tolerate without significant degradation of the performance. In addition, the high number (up to 200) of proton-proton collisions per bunch crossing (pileup) and the high number of generated particles require finer granularity and tracking

---

[1]The radiation damage from non-ionising energy loss (NIEL) in silicon sensors is dependent on the particle type, and is normally expressed as the equivalent damage of a fluence of 1 MeV neutrons (n$_{eq}$/cm^2).
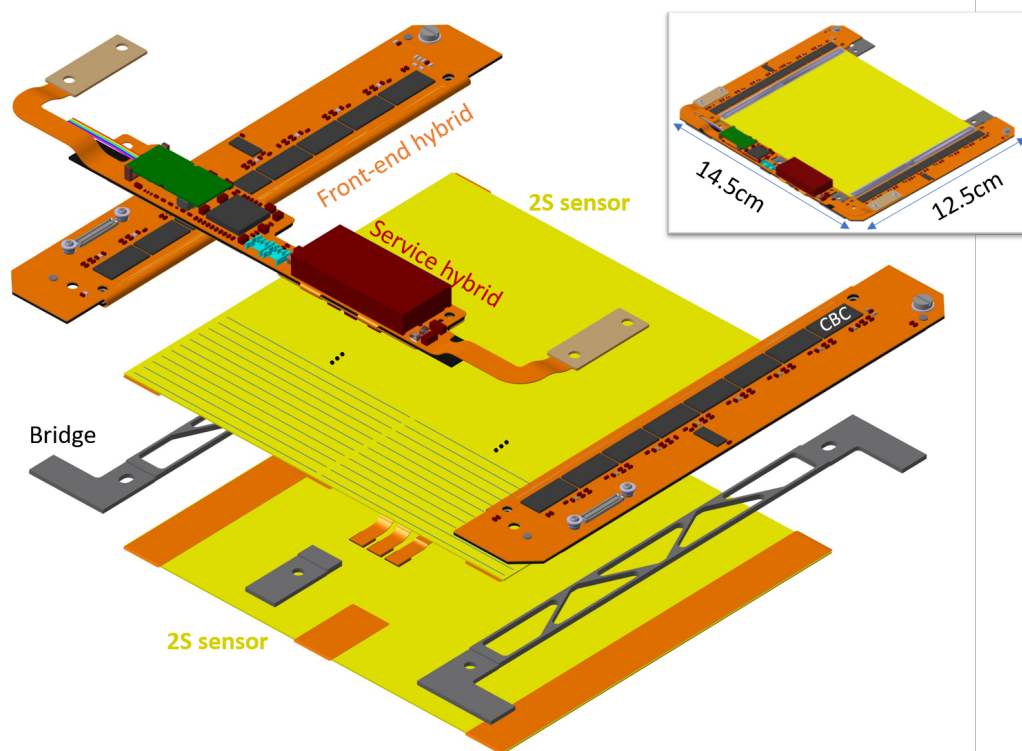
Figure 1. Exploded view of the 2S module. The completed module is shown in the insertion on the top right. The module consists of two 2S sensors (the strip segmentation is illustrated on the top sensor), which are glued to three bridges made of carbon fiber reinforced aluminum. The front-end hybrids on each end are connected via wire-bonds to the top and bottom sensors. The service hybrid implements the connection to the power system and the communication with the back-end system. Drawing after ref. [4].

information at the Level-1 trigger stage to efficiently select interesting events while limiting the trigger rate. These new requirements make it necessary to completely replace the tracking system of CMS with the Phase-2 Outer Tracker [4]. It should be noted that partial or entire replacement of the Phase-2 Outer Tracker will not be an option during the 10-year HL-LHC era.

For the Phase-2 Outer Tracker, three types of silicon sensors are assembled into two types of modules, which are both composed of a stack of two sensors with a separation that varies between 1.6 mm and 4 mm according to the position of the module in the detector. All Outer Tracker readout chips feature a binary readout scheme that records hits as binary 1 when the signal on the respective channel exceeds a programmable threshold. Modules for the outer region of the Outer Tracker contain two strip sensors read out by the CMS Binary Chips (CBC) [5, 6]. Both the outer region modules and the corresponding sensors are referred to as "2S". Figure 1 illustrates the composition of the 2S module including the two 2S sensors, bridges, front-end hybrids with the CBCs and a service hybrid for power and communication. The inner region is equipped with PS modules with one strip sensor (PS-s) and one macro-pixel sensor (PS-p). The sensors are read out by the Short Strip ASIC (SSA) [7] and Macro-Pixel ASIC (MPA) [8], respectively. The PS modules are conceptually similar to the 2S modules, but only half as long in the direction of the strips. The arrangement of the module types in the tracker is illustrated in figure 2. More details about the Outer Tracker module concept are given in ref. [9].
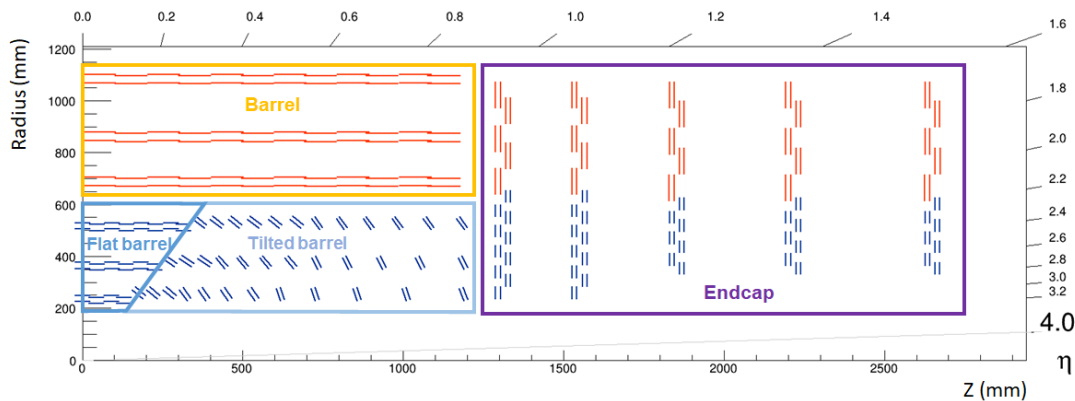
Figure 2. Cross-sectional view obtained by making a slice through one quadrant of the Phase-2 Outer Tracker at CMS in the *r*-*z* plane. The beam line is along the *z*-axis. The red lines represent 2S modules at larger radii and the blue lines the PS modules in the inner layers. These module types are described in the text below.

The silicon sensors will be exposed to severe radiation during the operation at the HL-LHC. The radiation-induced defects in the silicon substrate change the properties of the sensors. The leakage current increases and the induced signal decreases. To reduce the current in the silicon substrate and to prevent thermal runaway,[2] the modules are cooled and the sensors kept at a temperature of about $-20\,^{\circ}$C. The reduction of the signal is attributed to changes in the electric field inside the substrate and trapping of charge carriers. To overcome this effect the operating voltage can be raised from the nominal 600 V to 800 V to maintain a sufficiently large signal. At $-20\,^{\circ}$C the radiation-induced defects in the silicon substrate, and with them also the leakage current, are essentially stable with time. The operation schedule of the detector foresees maintenance periods at the end of each year. They can be exploited for intentional annealing of the defects in the silicon substrate at around room temperature. These annealing phases would have the beneficial effect of reducing the sensor current induced by radiation damage. The annealing of the defects also affects the charge collection of the sensors. The net effect depends on the annealing time: shorter exposure increases the signal, while longer annealing decreases it. Therefore, characterizing the annealing behavior of the signal is crucial to compare silicon sensor options for the Phase-2 upgrade.

Based on their prevalence in HEP experiments, it was always assumed that the sensors for the new Outer Tracker would be planar silicon with strip (or macro-pixel) implants on one side. Previous studies further determined that the sensors should be float-zone (FZ) silicon with n-doped strips and a p-doped substrate [10, 11]. The remaining choice to be made for the silicon sensors for the Outer Tracker was the active thickness. Thinner sensors promise several potential benefits like

- lower material budget,
- smaller total current at a given bias voltage because of a smaller active volume, and
- higher charge collection efficiency after irradiation at the same bias voltage because of higher electric fields leading to a faster drift of the charge carriers and therefore to a lower charge carrier trapping probability.

---

[2]A positive feedback loop between increasing current and increasing temperature leading to an exponential current increase.

An earlier study compared the performance of irradiated sensors made of FZ silicon of 320 μm thickness but different active thicknesses (200 μm, 240 μm, and 290 μm), obtained by deep-diffusion of the backside doping layer [4]. The results showed that sensors with an active thickness of 240 μm provide the highest signal over a wide range of annealing times.

After publication of this study, the fluence estimations were updated as a result of changes in the CMS detector geometry. In addition, physical thinning (by grinding and polishing) was selected to reduce the active thickness in place of deep-diffusion. As a result, the CMS Collaboration performed a direct comparison of the baseline material, which has a physical thickness of 320 μm and an active thickness of 290 μm, and the thinned 240 μm thick material. This paper describes the measurements performed and how the thickness was selected between the two options.

The paper is structured as follows. Section 2 provides a description of the sensors of the Phase-2 Outer Tracker, as well as details on the test sensors used for this study. The expected radiation environment of the Outer Tracker and the irradiations are described in section 3. The measurement procedures are covered in section 4, followed by the measurement results in sections 5, 6, and 7, which include the characterization of the sensor parameters, charge collection measurements, and beam tests. Additional aspects beyond sensor performance are discussed in section 8. Section 9 summarizes the main considerations leading to the final thickness choice.

2 Samples

Three designs of silicon sensors are used in the CMS Phase-2 Outer Tracker. All are of type n-in-p (highly n-doped strips in p-doped bulk) with p-stop strip isolation [10]. The 2S and PS-s sensors are AC coupled[3] strip sensors with about 2000 strips at a strip pitch of 90 μm and 100 μm, respectively. The outer dimensions of the 2S sensors are ~10 cm × 10 cm, while the PS-s sensors have dimensions of ~10 cm × 5 cm. For both sensors the strips are segmented in two halves each read out from the corresponding end of the sensor when assembled into a module. Figure 3 shows the schematic drawing of such a sensor type. The PS-p sensor has rows of very short strips (referred to as macro-pixels with 1.4 mm length) that directly connect the implants (DC coupling). The outer dimensions are nearly equal to those of the PS-s sensor.

The sensors must comply with the specifications set by the CMS Collaboration (table 1). Following a market survey, the only vendor compliant with the CMS requirements was Hamamatsu Photonics K.K. (HPK). The preferred material of this vendor is float zone (FZ) silicon with a physical thickness of 320 μm and an active thickness of 290 μm (referred to as FZ290 in this paper). The difference in the physical and active thickness comes from a special treatment that allows the backside doping in the sensors to extend for about 30 μm. This deep backside doping is also present in the current CMS tracker sensors (as p-in-n material) and proved to make the sensors less sensitive to minor scratches. Another important feature of the HPK material is the higher oxygen concentration compared to other FZ silicon providers (about 5 to 10 times more). This property is beneficial in terms of radiation hardness, as reported in ref. [13].

To investigate the benefits of thinner silicon material the baseline FZ290 sensors were compared to sensors made of thinned silicon material. The investigated material has a physical and active thickness of 240 μm and is referred to as thFZ240 in this paper.

---

[3]The metal readout strip is separated from the charge collecting implant by a thin dielectric layer.
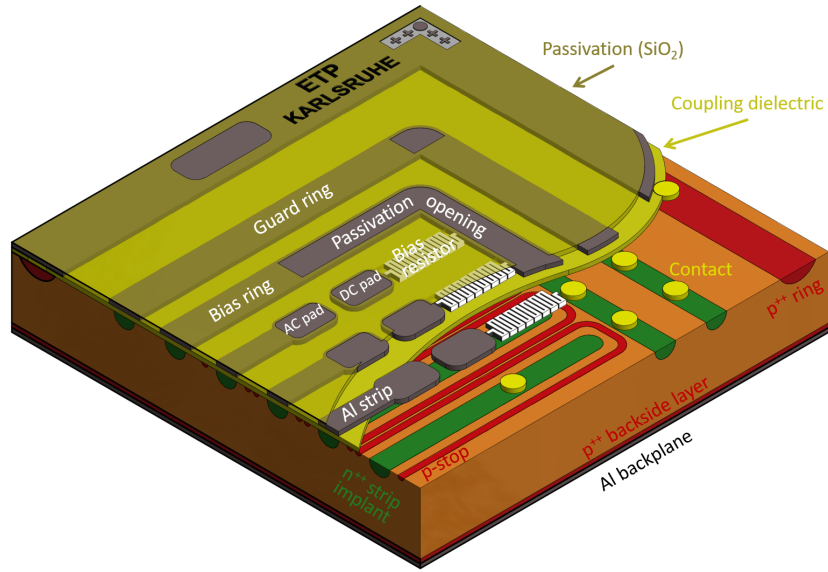
Figure 3. Schematic drawing of a portion of a p-type, AC coupled strip sensor similar to the ones used for the CMS Phase-2 Outer Tracker (after ref. [12]).

Table 1. Specifications for the qualification parameters of the CMS Outer Tracker sensors. Bad strips are defined by a failure of one or more of the strip parameter specifications.

Parameter	Specification
Full depletion voltage	$< 350\,V$
Current at 600 V	$\leq 2.5\,nA/mm^3$
Breakdown voltage	$> 800\,V$, $I_{800V} < 2.5 \times I_{600V}$
Strip current	$< 10\,nA/cm$
Bias resistor resistance	$1.5 \pm 0.5\,M\Omega$
Coupling capacitance	$> 1.2\,pF/(cm \cdot \mu m)$
Dielectric current (pinhole check)	$< 10\,nA$ at 10 V
Interstrip resistance	$> 10\,G\Omega\,cm$ (strip to one nearest neighbor)
Interstrip capacitance	$< 0.5\,pF/cm$ (strip to one nearest neighbor)
Number of bad strips	< 20

Instead of full-size sensors, as used in the final modules, AC coupled miniature strip sensors processed by HPK on wafers of the two material types (FZ290 and thFZ240) with the same mask set were mainly used in this study. Details of the sensor layout, dimensions, and process parameters are listed in table 2. The short sensors were used for the charge collection study (section 4.2), while the long sensors were assembled into mini-modules for a beam test (section 4.3).

3 Radiation environment and irradiation procedure

The expected radiation environment for the silicon sensors is derived from FLUKA simulations [14, 15] of the CMS detector. The nominal integrated luminosity used for this study is $3000\,fb^{-1}$, which

Table 2. Layout, dimensions, and process details of the miniature strip sensors. Values for the doping and oxide concentrations as well as the dielectric thickness are based on previous measurements of similar materials.

Parameter	Short sensor	Long sensor
Strip implant length (cm)	2.0	4.8
Strip implant width (µm)	22	
Strip pitch (µm)	90	
Strip metal width (µm)	32	
Number of strips	64	127
Number of guard rings	1	
Overall dimensions (cm^2)	2.3×0.8	5.0×1.4
Coupling dielectric thickness (nm)	~ 300 (SiO$_2$/Si$_3$N$_4$)	
Peak strip doping concentration (cm^{-3})	$\sim 1 \times 10^{19}$	
Peak p-stop doping concentration (cm^{-3})	$\sim 5 \times 10^{15}$	
Bulk doping concentration (cm^{-3})	$\sim 4 \times 10^{12}$	
Oxygen concentration (cm^{-3})	$\sim 5 \times 10^{16}$–1×10^{17}	

is the projected total after 10 years of operation at the HL-LHC. The 1 MeV neutron equivalent fluence in the tracker region is shown in figure 4. The radiation field is composed of different particle types (neutrons, protons, charged pions, and an "all particles" category that also includes electrons, positrons, muons, photons, etc.). This plot shows that the neutron fraction of particles increases with the distance from the interaction point. These fluence estimates were updated with respect to the Technical Design Report [4], and the new values are summarized in table 3. They show increased expected fluence values compared to figure 4 for some regions in the tracker. A detailed distribution of the fluences accumulated by the modules is shown in figure 5. Only a small fraction of the 2S and PS modules will receive an integrated fluence close to the maximum fluence for the 2S and PS regions listed in table 3. The range of fluences chosen for this irradiation campaign also covers the updated levels as outlined below.

Previous studies have shown that oxygen-rich silicon material exhibits different properties when exposed to charged particles than when exposed to neutral particles [13]. Since the investigated FZ material from HPK has a higher oxygen concentration than standard FZ material from other vendors, this irradiation campaign always includes two irradiation steps, one with charged hadrons and one with neutrons. The expected particle type ratio varies over the radial distance of the module position from the beam line, as illustrated in figure 4. Therefore, two mixtures of charged and neutral particle irradiation were chosen to represent the inner region (35% of neutral particles at a radius of about 20 cm; representative of PS module positions) and outer region (80% of neutral particles at a radius of about 65 cm; representative of 2S module positions).

The selected *maximum* fluences in this study for the inner and outer regions after 3000 fb^{-1} are 1×10^{15} n$_{eq}$/cm^2 and 3×10^{14} n$_{eq}$/cm^2, respectively, and are based on the simulations shown in figure 4. These fluences are complemented with a *low* fluence to check the performance after about 1000 fb^{-1}, and a higher fluence representing the expected maximum fluences for the *ultimate*
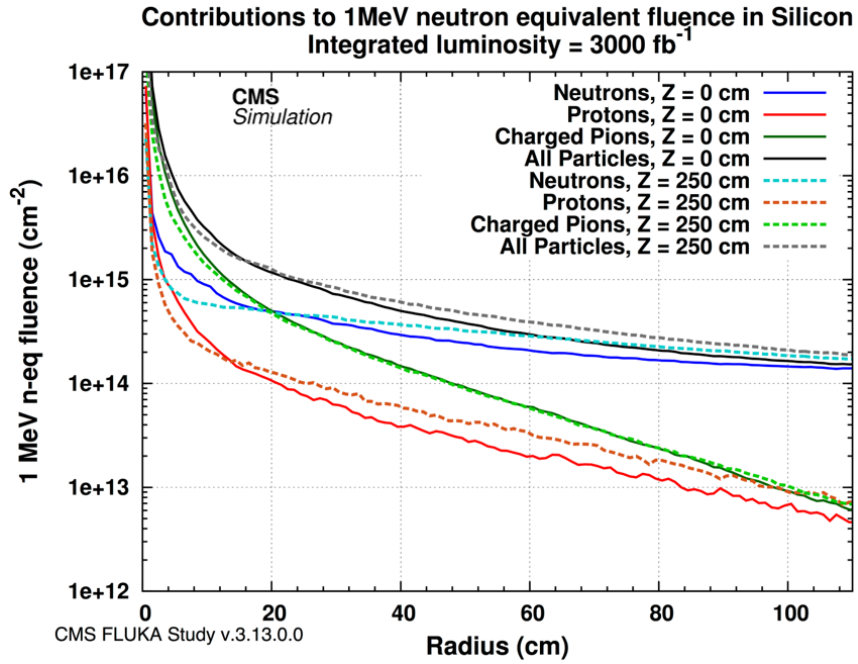
Figure 4. FLUKA v3.13.0.0 simulation results of the fluence levels in the CMS tracker after $3000\,\mathrm{fb}^{-1}$ of integrated luminosity as a function of radial distance from the beam line [16]. The z-position in the legend refers to the distance from the interaction point along the beam axis.

Table 3. Maximum fluence after $3000\,\mathrm{fb}^{-1}$ and $4000\,\mathrm{fb}^{-1}$ assigned to the different module types and their positions in the tracker based on FLUKA v3.7.20.1 simulation results. The radial and z coordinates of the position of the module that is expected to receive the highest fluence are provided in columns three and four.

| Type / location	No. of modules	z position (mm)	Radius (mm)	Max. module fluence (n_{eq}/cm^2)	
				$3000\,\mathrm{fb}^{-1}$	$4000\,\mathrm{fb}^{-1}$
1.8 mm 2S barrel	4416	1127	669	2.8×10^{14}	3.7×10^{14}
1.8 mm 2S endcap	2768	2239	768	2.9×10^{14}	3.8×10^{14}
4.0 mm 2S endcap	424	2643	665	3.7×10^{14}	4.9×10^{14}
4.0 mm PS endcap	2720	2673	355	8.5×10^{14}	11.3×10^{14}
1.6 mm PS flat barrel	826	135	347	6.0×10^{14}	8.0×10^{14}
2.6 mm PS flat barrel	126	129	218	10.5×10^{14}	14.0×10^{14}
2.6 mm PS tilted barrel	1336	268	252	8.8×10^{14}	11.7×10^{14}
4.0 mm PS tilted barrel	584	315	249	8.8×10^{14}	11.7×10^{14}
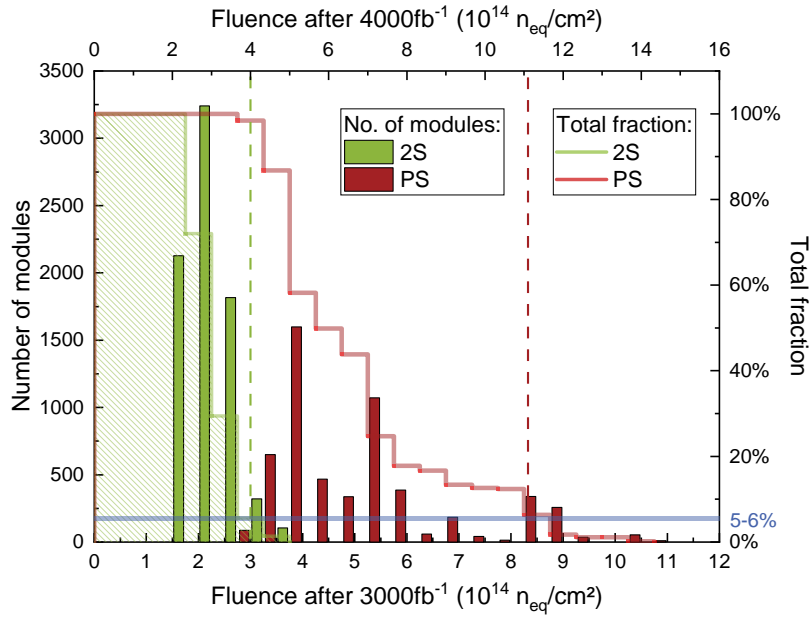
Figure 5. Distribution of the integrated fluence the modules will have received at the end of operation taking into account their locations in the CMS tracker. The lower *x*-axis indicates the fluence after $3000\,\mathrm{fb}^{-1}$ and the upper after $4000\,\mathrm{fb}^{-1}$. Besides the histogram of the number of modules for each accumulated fluence bin, the plot includes the integrated total fraction of modules whose accumulated fluence will exceed the corresponding fluence. The green and red dashed lines indicate the maximum fluences for about 95% of modules in the 2S and PS regions, respectively. The data are based on FLUKA v3.7.20.1 .

Table 4. Irradiations performed with the short sensors. At least two sensors of each thickness were irradiated to the mixed fluence in each row. These reflect the expected mixture of charged (protons) and neutral (neutrons) particles in the inner (at a radius of about $20\,\mathrm{cm}$) and outer (at a radius of about $65\,\mathrm{cm}$) part of the CMS Outer Tracker. In the last column F_n is the fluence of the pure neutron irradiation, while F_total is the total fluence. The highest fluence from table 3 in the default (ultimate) scenario is $3.7 \times 10^{14}\,\mathrm{n_{eq}/cm^2}$ ($4.9 \times 10^{14}\,\mathrm{n_{eq}/cm^2}$) for the 2S region and $10.5 \times 10^{14}\,\mathrm{n_{eq}/cm^2}$ ($14 \times 10^{14}\,\mathrm{n_{eq}/cm^2}$) for the PS region.

Region	Level	Neutrons $(\mathrm{n_{eq}/cm^2})$	Protons $(\mathrm{n_{eq}/cm^2})$	Total $(\mathrm{n_{eq}/cm^2})$	Neutron frac. $F_\mathrm{n}/F_\mathrm{total}$
PS $(R \sim 20\,\mathrm{cm})$	Low	1×10^{14}	2×10^{14}	3×10^{14}	~35%
	Maximum	4×10^{14}	6×10^{14}	10×10^{14}	~ 40%
	Ultimate	5×10^{14}	10×10^{14}	15×10^{14}	~ 35%
2S $(R \sim 65\,\mathrm{cm})$	Low	0.75×10^{14}	0.25×10^{14}	1×10^{14}	~75%
	Maximum	2.5×10^{14}	0.5×10^{14}	3×10^{14}	~80%
	Ultimate	5×10^{14}	1×10^{14}	6×10^{14}	~80%

performance scenario of the HL-LHC with an integrated luminosity of $4000\,\mathrm{fb}^{-1}$. The selected fluences were aligned with those used in previous studies. The resulting irradiation plan is shown in table 4. The fluence levels in table 4 corresponding to the *maximum* level exceed the fluences expected by 95% of the modules in the respective regions for the default luminosity scenario.

Considering annealing aspects, the detector could be kept at room temperature (approximately +20 °C) during the maintenance periods at the end of each year of operation, which are typically two weeks long. In this way the sensors could accumulate 20 weeks of annealing time by the end of the HL-LHC period after ten years of operation, which would reduce the leakage current of the sensors and therefore also the dissipated power. Therefore the scenario of 20 weeks of annealing at room temperature is a benchmark for the following studies in this paper, while up to 30 weeks is still a possibility.

Proton irradiations were performed at the Karlsruhe compact cyclotron (KAZ) with a proton energy of 23 MeV [17] and at the MC40 cyclotron of the University of Birmingham with a proton energy of 24 MeV [18]. The uncertainty of the delivered fluence is estimated to be about 15% and the used hardness factor converting the proton fluence into the fluence equivalent to 1 MeV neutrons is 2.0. At both facilities the irradiations lasted less than 30 minutes and the samples were kept below 0 °C during the irradiation. Afterwards the samples were stored in a freezer at temperatures below −18 °C.

The neutron irradiations of the miniature sensors were performed at the TRIGA reactor of the Josef Stefan Institute (JSI), Ljubljana [19]. The uncertainty of the delivered fluence is estimated to be less than 10% and the hardness factor was reported as 0.9 [20]. The irradiation time was around 10 minutes, but the samples were not cooled and could reach temperatures of up to +40 °C. Following irradiation the sensors were kept nearby at room temperature for an hour to allow for the decay of short-lived isotopes before being moved to a freezer. Full-size sensors were irradiated at the Rhode Island Nuclear Science Center (RINSC [21]), Rhode Island, which is a reactor similar to the one at JSI, and similar procedures were applied. For irradiations with both particle types the irradiation with neutrons was always first.

The KAZ was used for irradiating all of the FZ290 samples. Because of a technical problem with the KAZ the proton irradiation of the thFZ240 sensors was done at the MC40 cyclotron. After preliminary completion of the study, the KAZ became available again and a few thin sensors were irradiated also with KAZ protons and the performance was compared to the sensors irradiated with the nominally equivalent MC40 protons. This comparison is presented in section 6.

The long miniature strip sensors used for the beam test have been irradiated at JSI only, since the KAZ was not available for these as well. The sensors were irradiated before being assembled into modules. The readout ASICs were not irradiated. The radiation tolerance of the readout chips was studied in refs. [7, 8, 22] and indicated no problems for the module performance.

An overview of the irradiation sites used in the sensor thickness study is given in table 5. In order to be able to cross-check results two miniature sensors of each type were always irradiated together (in the same scan area or irradiation tube) to a given fluence.

4 Measurement procedures

In this section the procedures are described that were applied for the various measurements conducted during this study.

Table 5. Overview of the used irradiation sites for the different samples. The (×) for the short thFZ240 sensors indicates the later irradiations performed at KAZ for cross-checks.

Sensor type	23 MeV protons KAZ	24 MeV protons MC40	Neutrons JSI	Neutrons RINSC
Short FZ290 sensors	×		×	
Short thFZ240 sensors	(×)	×	×	
Long FZ290 sensors			×	
Long thFZ240 sensors			×	
Full-size FZ290 sensors	×			×

Table 6. Details of the measurement procedures for the sensor characterization. Chuck temperatures are +20 °C and −20 °C for non-irradiated and irradiated samples, respectively. An LCR meter is an impedance analyzer named for its inductance (L), capacitance (C), and resistance (R) measurement functions. It can be operated at different test frequencies, as indicated in the table. The guard ring is left floating for all tests.

Measurement type	Contact(s)	Comment
Current vs. voltage	bias ring	from 0 to 1000 V in 10 V steps
Capacitance vs. voltage	bias ring	from 0 to 600 V in 10 V steps at 1 kHz
Coupling capacitance	AC&DC pads	LCR meter frequency of 1 kHz
Bias resistance	DC pad	current difference between 0 and 2 V
Strip leakage current	DC pad	
Pinhole test	AC&DC pad	AC pad current at 10 V
Interstrip capacitance	2 DC pads	LCR meter frequency of 1 MHz
Interstrip resistance	2 DC pads	extracted from a 0 to 5 V ramp

4.1 Sensor characterization

The basic sensor parameters are measured in semi-automated probe stations using needle probes. The samples are placed on a temperature-controlled chuck, which has a series of small holes for holding the sensors in place by vacuum. The chuck also provides the high potential of the negative biasing voltage. The bias ring on the top-side of the sensor is connected to the ground potential via a needle connection. This is the configuration for global current versus voltage (IV) or capacitance versus voltage (CV) measurements. Up to two more needles are required to connect the pads of individual strips for strip specific measurements like coupling capacitance, bias resistance, strip leakage current, and current through the dielectric (pinhole test). Two needles placed on neighboring contacts are required for the measurements of interstrip capacitance and interstrip resistance. Further details of the measurement procedures are given in table 6.
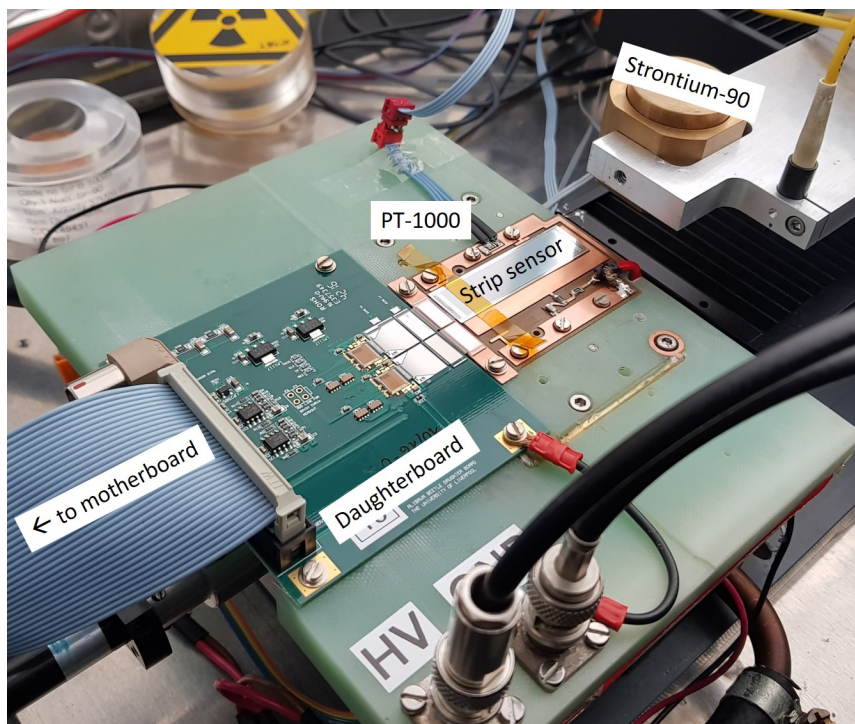
Figure 6. The ALiBaVa setup at KIT with one of the long miniature strip sensors on the PCB. The strontium-90 source is moved above the sensor for the measurements. Details about the setup are provided in the text below.

4.2 Charge collection measurements

To obtain the collected charge in response to minimum ionizing particles the ALiBaVa[4] system [23, 24] was used to read out the signals from the sensors. Figure 6 shows a picture of the setup. The ALiBaVa readout system uses the Beetle readout chip [25], which provides analog signals with a 50 ns shaping time, compatible with the LHC 25 ns bunch crossing time. For biasing and cooling the sensors are mounted on a PCB, which is fixed to a cooled copper block. The cooling is provided by a water glycol chiller for pre-cooling and a second stage with Peltier elements. This way the sensor can be cooled down to $-20\,°C$ for the measurements, but also heated up to $+80\,°C$ for annealing of radiation-induced defects without removing the sensor from the chuck. The sensor is wire-bonded to a daughterboard hosting the Beetle chips. The daughterboard is connected to an FPGA-based motherboard for data acquisition and communication with a readout PC. The setup is equipped with a strontium-90 source (emitting electrons with an energy up to 2.3 MeV) above the sensor and a scintillator with a photomultiplier tube is placed below the sensor to trigger on passing particles. The source is shielded by a collimator with an opening diameter of 0.8 mm and a thickness of 8 mm, which allows a maximum deviation from normal incidence of 5°. The resulting hit distribution on the sensor has a FWHM of about 20 strips. A bias voltage ramp from 300 to 900 V in 100 V steps is performed. This is repeated after each of the nine annealing steps summarized in table 7. The current-related damage rate coefficient α is used as a basis for comparing different annealing times and temperatures. This parameter is defined as $\alpha = \Delta I/(V \cdot F)$, where ΔI is the current increase

---

[4]A Liverpool Barcelona Valencia readout system

Table 7. Incremental annealing steps for the charge collection measurements. Equivalent annealing times (corresponding to the same fractional decrease in leakage currents) at +21 °C are also included in the last row.

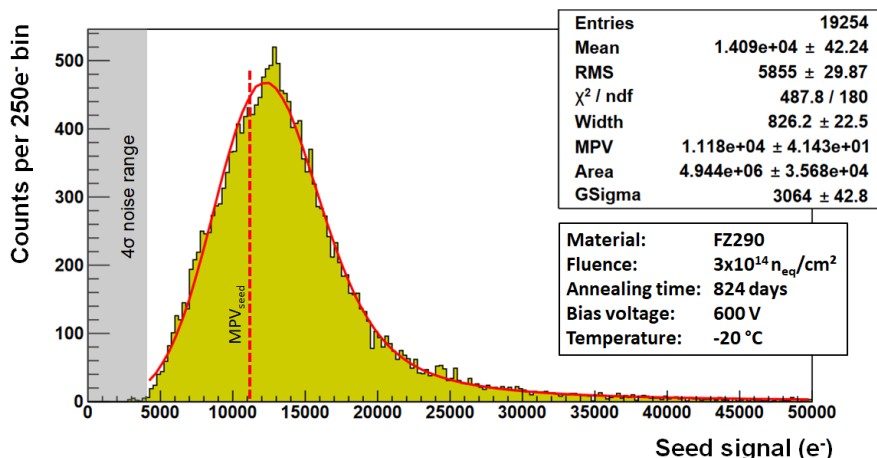| Step	1	2	3	4	5	6	7	8	9
Temperature (°C)	+60	+60	+60	+60	+60	+60	+80	+80	+80
Time (min)	10	20	40	80	100	140	25	57	120
Eq. time at +21 °C (days)	3.8	6.9	13.3	27.9	53.7	100.0	203.1	407.4	824.1

Figure 7. Example of the pulse height distribution in electrons of seed signals fitted by a convoluted Landau-Gauss function as measured with the analog ALiBaVa readout system. The gray area indicates the 4σ noise range, which corresponds to four times the typical strip noise, the minimum threshold at which the CBC is operated (section 6). The dashed red line indicates the $\mathrm{MPV_{seed}}$ value of the (pre-convoluted) Landau distribution.

after irradiation (approximately the current after irradiation, since the initial current is very low), V is the active volume and F the particle fluence. The current-related damage rate of a given annealing history (steps with duration and temperature) is calculated according to the parametrization given in ref. [26]. The time that would be required at +21 °C to reach that accumulated α is calculated and quoted as "eq. time at +21 °C" in table 7.

For each sensor condition (bias voltage and annealing) several measurements are performed: the noise and pedestal are determined from a run with random triggers, a gain calibration is performed using internal calibration pulses, and finally hit events, triggered by traversing electrons from the strontium-90 source, are recorded in order to determine the charge collection. More details can be found in ref. [27]. The seed signal, defined as the highest strip signal within a cluster of consecutive strips, is used for further analysis. This approach was chosen since the final readout chips will feature a binary readout, and only signals exceeding a programmable threshold are recorded as hits. The most probable value of the seed signal height ($\mathrm{MPV_{seed}}$) is derived from a fit to the seed signal height distribution using a convoluted Landau-Gauss function [28], for which an example is shown in figure 7. The chosen function provides a good description of the distribution, and the resulting $\mathrm{MPV_{seed}}$ serves as a conservative estimator of the seed signal strength to compare the performance of the two materials under the different conditions.
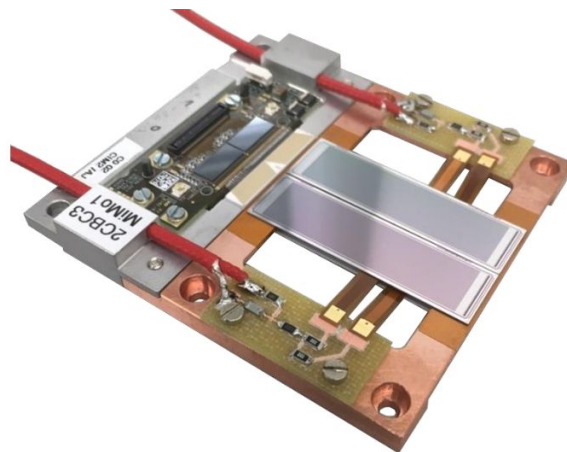
Figure 8. One of the three mini-modules assembled for the DESY beam test.

The procedure of initial irradiation followed by consecutive annealing steps does not exactly reflect the operation scenario, for which the yearly radiation portion is followed by an annealing period during the technical stop. The performed measurement procedure results in an overestimation of long-term effects, since all defects are exposed to the long annealing times. A study is underway to quantify the potential difference with respect to an HL-LHC scenario. For the present comparative study the difference is not relevant.

4.3 Characterization of sensors in test beams

In May 2019, a beam test was conducted at DESY (Deutsches Elektronen-Synchrotron) in Hamburg, Germany. The beam test complemented the charge collection results obtained with the analog readout in laboratory tests with hit efficiency measurements with the almost final front-end chip implementing a binary readout scheme. The test beam facility at DESY provides electrons or positrons at energies up to 6 GeV [29].

The particle beam was configured to deliver electrons at an energy of 5.6 GeV, which yielded a trigger rate of 500 to 700 Hz. The TB21 beam line was used, which is equipped with the DATURA hodoscope [30] based on MIMOSA CMOS pixel sensors [31].

Three 2S mini-modules were built for the beam test. Each module was composed of four mini-strip sensors (long type in table 2), two sensors of the FZ290 material and two of the thFZ240 material. The sensors are arranged in two layers mimicking the 2S module design. A picture of one mini-module is shown in figure 8. Thick (thin) sensors are assembled with a spacing[5] of 1.8 mm (1.7 mm). Each module is equipped with two CBCs (v3.0). Each CBC reads out 127 strips from the top sensor and 127 strips from the bottom sensor [4]. In the mini-modules one CBC therefore records signals from pairs of sensors of the same thickness. All sensors of one module were exposed to the same fluence of reactor neutrons (2.5×10^{14} n_{eq}/cm^2 or 5.0×10^{14} n_{eq}/cm^2, which corresponds to the *maximum* and *ultimate* neutron fraction of the 2S irradiation plan from table 4). The sensors of each thickness were annealed to two different equivalent annealing times at +21 °C (13.3 days and 203 days including 4 days of assembly time at room temperature). Table 8 summarizes the

---

[5]Spacing defined as distance between the center planes of the sensors.

Table 8. Irradiation fluence levels and equivalent annealing time at +21 °C for the long type sensors of the mini-modules investigated in the DESY beam test.

Mini-module	Position	Sensor material	Fluence (n_{eq}/cm^2)	Eq. time at +21 °C (days)
MiMo1	top, right	FZ290	0	–
	bottom, right	FZ290	0	–
	top, left	thFZ240	0	–
	bottom, left	thFZ240	0	–
MiMo2	top, right	FZ290	2.5×10^{14}	13
	bottom, right	FZ290	2.5×10^{14}	203
	top, left	thFZ240	2.5×10^{14}	13
	bottom, left	thFZ240	2.5×10^{14}	203
MiMo3	top, right	FZ290	5.0×10^{14}	13
	bottom, right	FZ290	5.0×10^{14}	203
	top, left	thFZ240	5.0×10^{14}	13
	bottom, left	thFZ240	5.0×10^{14}	203

fluences and equivalent annealing times for all twelve sensors that were used for the three modules. For the data taking, the irradiated modules were cooled down to −20 °C to keep the leakage current at acceptable levels and to prevent thermal runaway. The unirradiated module was operated at room temperature. A housing shielded the modules from light and was flushed with dry air to prevent condensation on the modules. Condition parameters like the module temperature, sensor bias voltage, and the leakage current were continuously monitored and recorded. The parameters varied during the beam time were the hit comparator threshold, the sensor bias voltage, and the beam incidence angle. In addition, measurements without beam were conducted to determine the noise, pedestal, and noise hit occupancy[6] of the modules. In a first step the recorded raw hit information has been processed using the EUTelescope framework [32]. From the clustered hit information on the hodoscope planes the EUTelTestFitter algorithm [33] reconstructs the tracks. The EUTelescope software aligns all hodoscope planes and the devices under test (DUTs) using the particle tracks. The mechanical alignment precision of the sensors within one module is worse than the software-based alignment in the beam. Thus, the four sensors of each module have been aligned as individual DUTs to improve the alignment precision. The interpolation of the tracks to the DUTs yields the expected hit position. A custom framework makes use of the high level tracking and hit information for the efficiency analysis. The following selection criteria are applied prior to the hit efficiency analysis to select valid tracks and identify the corresponding DUT hits:

a) Only tracks whose projections intersect the sensitive region of the DUT after alignment are accepted.

b) Noisy strips with a hit occupancy above 1.5 %, the first two edge strips (on either side) and strips with missing bond connection to the CBC are masked.

---

[6]Fraction of firing channels per triggered event in absence of injected signal.
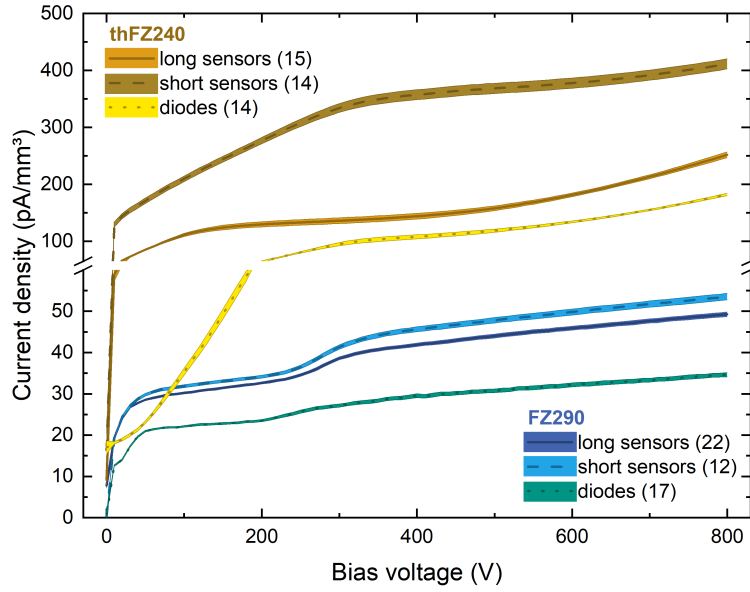
Figure 9. Averaged IV curves for mini-sensors and diodes prior to irradiation measured at +20 °C. The currents are normalized to the active volume of the devices. The numbers in the legend refer to the number of samples used to generate the averaged curve. For each bias voltage and sensor type the mean and standard deviation of the measured current was computed. The mean is plotted as the line and the bands represent one standard deviation.

c) Tracks pointing to masked strips within a window of ±45 μm are rejected.

d) A cluster[7] is accepted for the efficiency calculation if its residual fulfills $|\Delta s| \leq 180\,\mu m$, which is two times the strip pitch. The residual Δs is the distance between the cluster center and the expected track position on the DUT.

The efficiency η is finally calculated by

$$\eta = \frac{n_{\text{matched clusters}}}{n_{\text{valid tracks}}} \tag{4.1}$$

with the number of valid tracks $n_{\text{valid tracks}}$ following criteria a) to c) and the number of matched clusters $n_{\text{matched clusters}}$ (including single hits) following selection d). The uncertainty is defined as

$$\sigma_\eta = \sqrt{\frac{\eta \cdot (1 - \eta)}{n_{\text{valid tracks}}}}. \tag{4.2}$$

5 Results of the sensor characterization

The miniature strip sensors were characterized prior to irradiation using the probe station with the chuck temperature set to +20 °C. The full depletion voltage was derived from CV measurements and is about 265 V for the thick sensors and 195 V for the thin ones. Figure 9 shows the IV curves of several mini-strip sensors and diodes. The currents are generally very low compared to the

---

[7]Consecutive hit strips form a cluster.

Table 9. Typical strip parameter values of the short-strip sensors for the two thicknesses before irradiations. Interstrip parameters are measured to one neighbor only. The corresponding specifications for full-size sensors are listed in the last column. The short-strip sensors have anomalously high interstrip capacitance values (in fact equal to the full-size sensor limit by coincidence) because of a geometric feature of the mini-sensors: the contribution of the pad area (with larger capacitance) to the total capacitance is larger than for the longer strips of full-size sensors.

Parameter	FZ290	thFZ240	Specifications
Coupling capacitance (pF/cm)	30	28	> 24
Bias resistance (MΩ)	1.9	1.8	1-2
Strip leakage current (pA/cm)	4–7	10–30	< 10000
Interstrip capacitance (fF/cm)	500	500	< 500
Interstrip resistance (GΩ cm)	>1000	>800	>10

specifications given in table 1 and the spread of the IV curves is very small, as indicated by the narrow bands representing the standard deviations of the measured currents at each voltage point. The thinned mini-sensors show a higher leakage current, which might be related to the thinning process. Table 9 summarizes typical values of the measured strip parameters. Most parameters are well within the specifications, and only the interstrip capacitance is close to the specified limit. The total interstrip capacitance consists of a contribution of the pad region with wider implants and higher capacitance, and the strip region with a lower capacitance. The relative contribution of the pad region, which has the same layout as for the full-size sensors, is higher on these mini-sensors. This is therefore not an issue for the 5 cm long strips of the full-size 2S sensors. The PS-s sensors, with their 2.5 cm long strips, might however come close to this non-critical limit. These measurements confirm the very high quality of the miniature strip sensors prior to irradiation.

After mixed irradiation (table 5) and annealing for 70 minutes at +60 °C (step 3 in table 7) the currents at 600 V normalized to the active volume are plotted versus the irradiation fluence for the two thicknesses in figure 10. From these plots the current-related damage rate α can be extracted. The α value at 600 V of the thick material is $\alpha = 4.9 \times 10^{-17}$ A/cm. The value is 15% larger than the estimate based on ref. [26] ($\alpha = 4.2 \times 10^{-17}$ A/cm) and has to be accounted for in thermal studies. The thin sensors could instead be operated at 400 V to yield an electric field similar to the electric field in thick sensors operated at 600 V. The α value of 4.4×10^{-17} A/cm obtained at 400 V is much closer to the expectation from literature than the one obtained for a bias voltage of 600 V. Above depletion, the electric fields are higher in thin material for the same bias voltage and the IV curves do not flatten out, as shown in figure 11.

In preparation for the beam test, eight long miniature strip sensors were characterized after pure neutron irradiation to 2.5×10^{14} n_{eq}/cm^2 and 5×10^{14} n_{eq}/cm^2 and for two different annealing conditions. The annealing was performed for 50 minutes at +60 °C (equivalent to about 9 days at +21 °C) for the "short" annealing and in several steps for a total of 156 minutes at +60 °C plus 45 min at +80 °C (equivalent to about 200 days at +21 °C) for the "long" annealing. No additional bad strips were identified after irradiation. Sensors that received a higher fluence show the expected higher strip leakage current, as shown in figure 12, and longer annealing durations reduce the currents, as expected. The coupling capacitance shows a slightly higher value (by about 2 pF) for the sensors
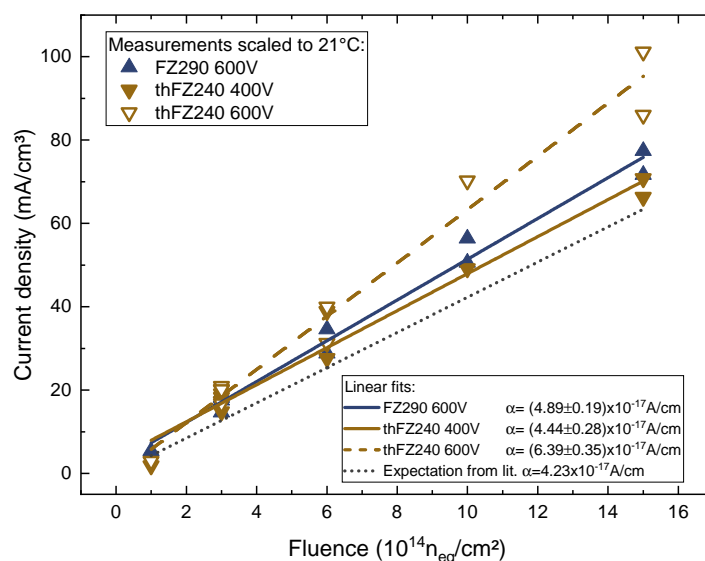
Figure 10. Current normalized to active volume after mixed irradiation of all short sensors. The measurements were performed at a temperature of −20 °C and the data scaled to +20 °C according to ref. [34]. The solid symbols are for the envisaged operation voltage (600 V for FZ290 and 400 V for thFZ240) while the open symbols indicate the increased currents for thin sensors at 600 V bias voltage. The lines represent linear fits to the data points, and are used to extract the current-related damage rate. The dotted line is an expectation from ref. [26].

exposed to the higher fluence as compared to those subject to the lower fluence, as shown in figure 13, where the annealing has no clear effect, and all values lie in a small band of 5 pF width. The bias resistance (figure 14) is slightly increased compared to the pre-irradiation values. This is mainly attributed to the lower measurement temperature, which increases the resistance of the polysilicon (0.4 %/K was measured in ref. [35]). The bias resistance was not measured for the sample with the higher fluence, but previous studies with HPK material showed no effect of irradiation on the bias resistance [11]. Mean measurement results from figures 12-14 are summarized in table 10.

To complement the measurements on miniature strip sensors, also four 2S full-size FZ290 sensors were irradiated, with one particle type each, and evaluated. Two of them were irradiated with protons at the KAZ ($F = 4.6 \times 10^{14}$ n$_{eq}$/cm^2) and two with neutrons at RINSC ($F = 4.2 \times 10^{14}$ n$_{eq}$/cm^2) (section 3). The current of the full-size sensor is an important ingredient to the thermal performance of the final modules and therefore the scaling of the leakage current from mini-sensors to the full-size sensors was checked. Figure 15 shows the currents of the four irradiated 2S sensors measured at −20 °C and 600 V as a function of the annealing time. Within the uncertainties the data agree with the currents calculated from ref. [26] using the stated fluences, a volume of 2.9 cm^3 and the current scaling factor from +21 °C to −20 °C of 1/64.6. The uncertainties include contributions from the absolute temperature (±0.5 °C) and fluence (±15%) determinations.

In addition, strip parameters were validated after irradiation for the two sensors irradiated with protons, and the results, summarized in table 11, show no significant deviations from pre-irradiation values, except for the expected radiation damage related increase in leakage current and decrease in interstrip resistance.
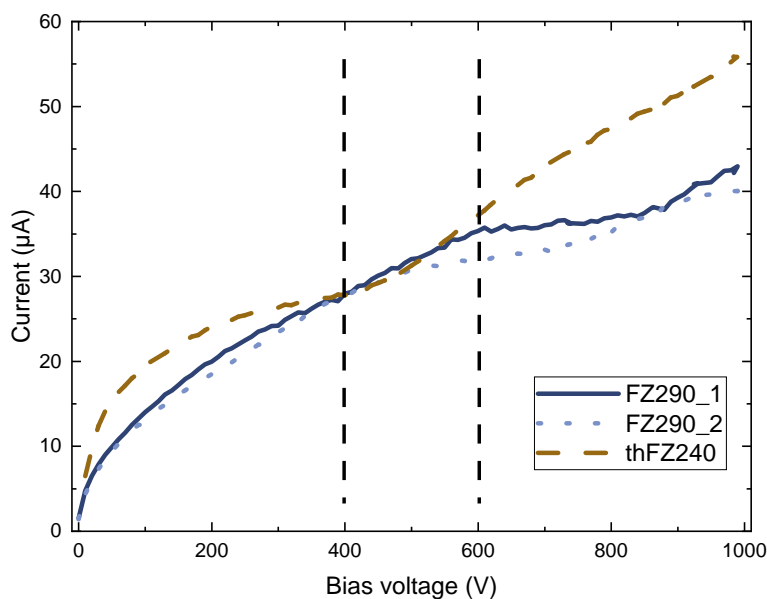
Figure 11. Comparison of the current vs. voltage characteristics for one thin (thFZ240) and two thick (FZ290) sensors irradiated to 1×10^{15} n_{eq}/cm^2. The measurements were performed at $-20\,°C$. The vertical lines indicate the bias voltages discussed in the text.
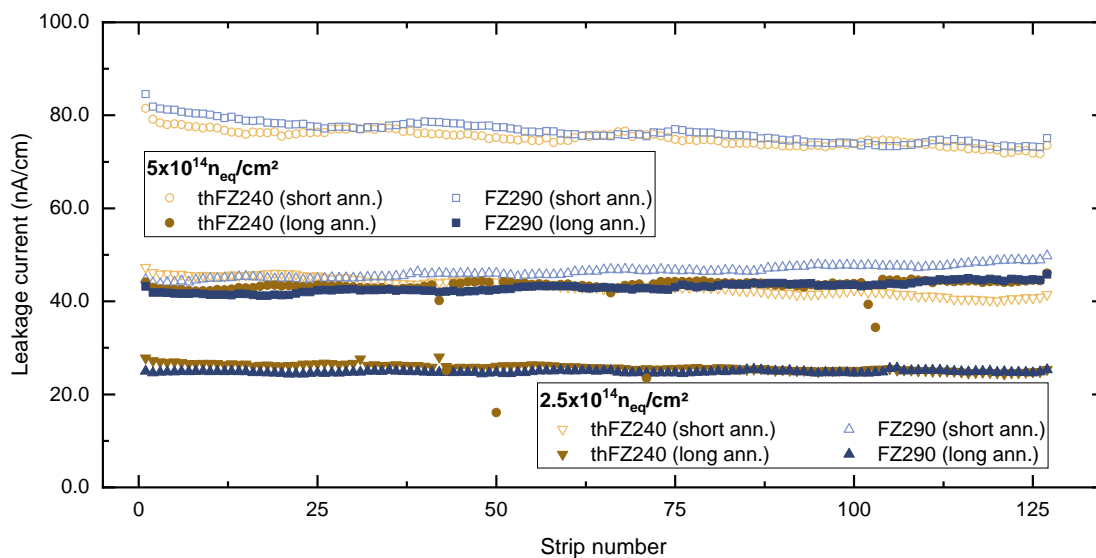

Figure 12. Leakage current vs. strip number measured at $-20\,°C$ and $350\,V$. The terms "short ann." (equivalent to 9 days at $+21\,°C$; open symbols) and "long ann." (equivalent to 200 days at $+21\,°C$; bold symbols) refer to the annealing time prior to the measurements. The data after a fluence of 2.5×10^{14} n_{eq}/cm^2 are represented by triangles and the data after 5×10^{14} n_{eq}/cm^2 with squares and circles.
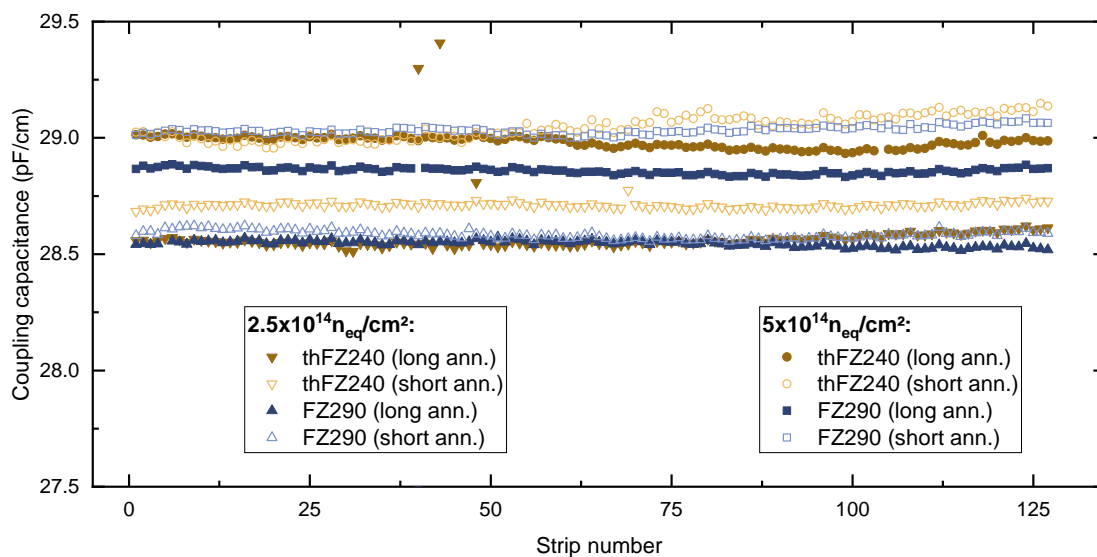
Figure 13. Coupling capacitance vs. strip number measured at $-20\,°C$ and $300\,V$ for the larger fluence set and $350\,V$ for the lower fluence set. The terms "short ann." (equivalent to 9 days at $+21\,°C$; open symbols) and "long ann." (equivalent to 200 days at $+21\,°C$; bold symbols) refer to the annealing time prior to the measurements. The data after a fluence of $2.5 \times 10^{14}\,n_{eq}/cm^2$ are represented by triangles and the data after a fluence of $5 \times 10^{14}\,n_{eq}/cm^2$ with squares and circles.
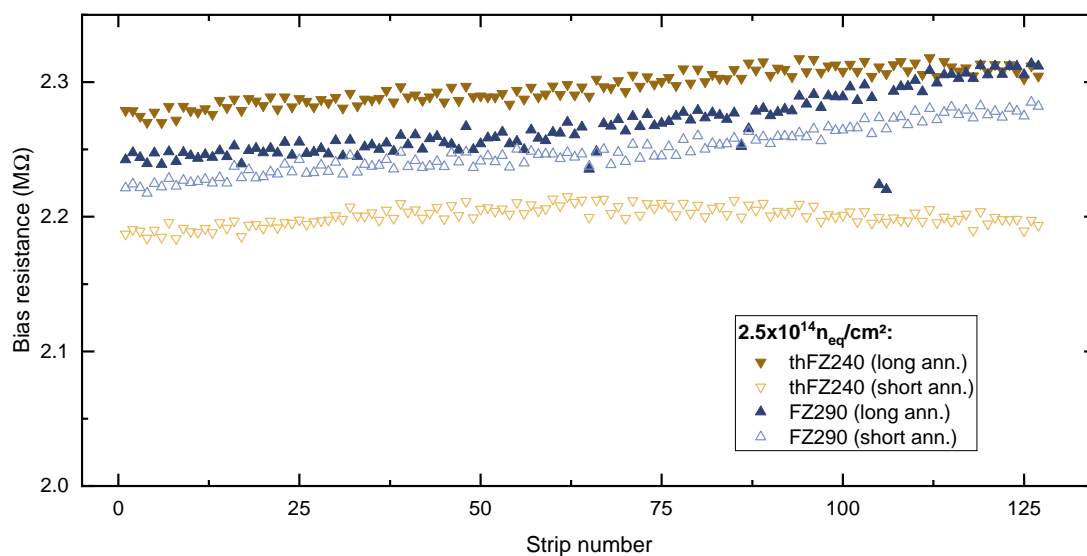

Figure 14. Bias resistance vs. strip number measured at $-20\,°C$ and $350\,V$. The terms "short ann." (equivalent to 9 days at $+21\,°C$; open symbols) and "long ann." (equivalent to 200 days at $+21\,°C$; bold symbols) refer to the annealing time prior to the measurements.

Table 10. Mean strip parameter values of the miniature strip sensors for the two thicknesses after irradiation with neutrons to 2.5×10^{14} n_{eq}/cm^2 with long annealing. The measurements were performed at $-20\,°C$. The corresponding specifications for full-size sensors are listed in the last column. The specification for the strip leakage current after irradiation is not defined. The interstrip parameters were only measured on short strip sensors and the measurements after 6×10^{14} n_{eq}/cm^2 at $600\,V$ were added in the lower half of the table for completion.

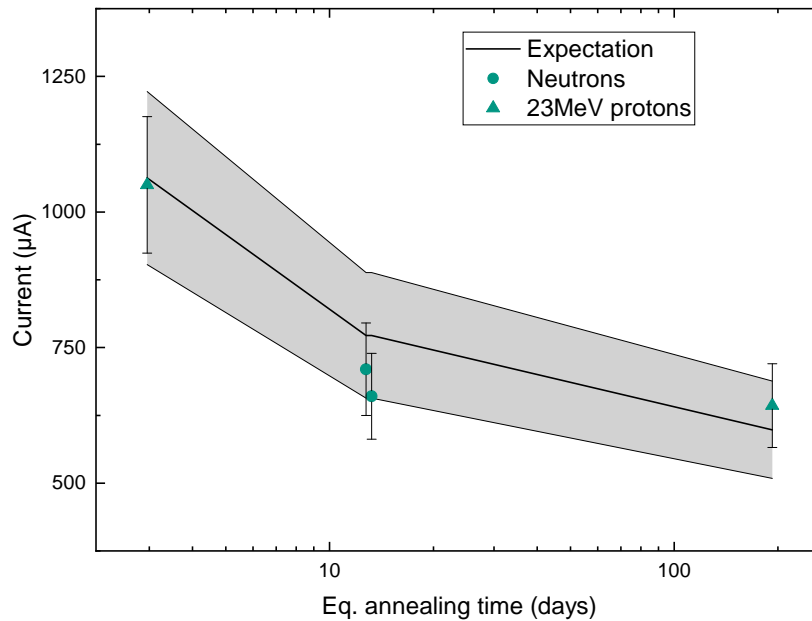| Parameter	FZ290	thFZ240	Specifications
Coupling capacitance (pF/cm)	28.5 ± 0.6	28.6 ± 0.1	> 24
Bias resistance (MΩ)	2.27 ± 0.02	2.30 ± 0.01	1–2
Strip leakage current (pA/cm)	24800 ± 200	25800 ± 700	–
Interstrip capacitance (pF/cm)	*0.45 ± 0.01*	*0.46 ± 0.01*	*< 0.5*
Interstrip resistance (GΩ cm)	*> 1*	*> 0.25*	*> 0.1*

Figure 15. Currents measured at $-20\,°C$ and $600\,V$ of the four irradiated full-size 2S sensors of type FZ290 over an estimated room temperature annealing time. The measurement of the temperature has an uncertainty of $\pm 0.5\,°C$, which propagates into the indicated uncertainty of the current at $-20\,°C$. The expectation is calculated from the current-related damage rates given in ref. [26] with an uncertainty (indicated as grey band) on the fluence of $\pm 15\%$. The two circles representing the two sensors irradiated with neutrons have the same annealing time but are displaced in the plot for clarity.

Table 11. Mean strip parameter values with standard deviations at 600 V for the two full-size 2S sensors (FZ290) irradiated to 4.6×10^{14} n_{eq}/cm^2 with 23 MeV protons. Interstrip parameters are measured to one neighbor only. The interstrip capacitance measurements for sensor 1 were performed with a bad calibration, and are omitted here. The specification for the strip leakage current after irradiation is not defined.

Parameter	Sensor 1 (200 days equiv. ann.)	Sensor 2 (3 days equiv. ann.)	Specifications
Coupling capacitance (pF/cm)	29.2 ± 0.2	29.2 ± 0.2	> 24
Bias resistance (MΩ)	2.3 ± 0.1	2.3 ± 0.1	1–2
Strip leakage current (nA/cm)	56.2 ± 5.0	92.8 ± 15.4	–
Interstrip capacitance (fF/cm)	–	322.0 ± 28.0	< 500
Interstrip resistance (GΩ cm)	4.1 ± 1.2	2.8 ± 1.1	> 0.1

In conclusion, the measurement results in this section did not show a significant difference between sensors of the two investigated thicknesses. Strip parameters are fulfilling the specifications for sensors of both thicknesses also after irradiation and also the leakage currents are similar if the operation voltage is adjusted based on the thickness.

6 Results of the charge collection study

Prior to installing sensors in the experiment the hit efficiency of a sensor can only be determined in beam test experiments, which are costly and time-consuming. A setup like the one presented in section 4.2, on the other hand, is well suited for characterizing a large number of samples. The results of charge collection studies can therefore be used to estimate the hit efficiency of the sensor. The CMS Collaboration is aiming for a minimum hit efficiency of 99.5 % on the active sensor region as a requirement for the tracker. In order to achieve such an efficiency, the generated signal of a sensor needs to be well above the threshold set in the readout chip. A readout threshold of four times the noise σ is usually sufficient to reduce the number of noise hits to an acceptable level. Therefore, 99.5 % of the signals need to be above this threshold. From the typical shape of the seed signal distribution from ionizing particles (figure 7) it can be estimated that the most probable value of the seed signal distribution should be three times larger than the threshold. The relation can be written as

$$\text{MPV}_{seed} > 3 \times 4\sigma = 12\sigma. \tag{6.1}$$

The 12σ-limit is an approximation and was introduced during the Phase-2 R&D process by the CMS Outer Tracker Sensor Working Group. Information about the three readout chips that are used in the CMS Phase-2 Outer Tracker is given in table 12. The SSA will read out the PS-s sensors and the MPA the PS-p sensors. The threshold for the MPAs is very low, which is related to the much lower capacitance of the small macro-pixels, and therefore the limit will not appear in the following plots. The noise of these chips can decrease at lower temperatures as foreseen during the operation in the experiment. This would add additional margin to the signal limit defined so far.

For the outer region covered with 2S modules a minimum MPV of the signal of 12 000 e^- is required. Figure 16 shows the measured seed signal versus the equivalent annealing time, focusing
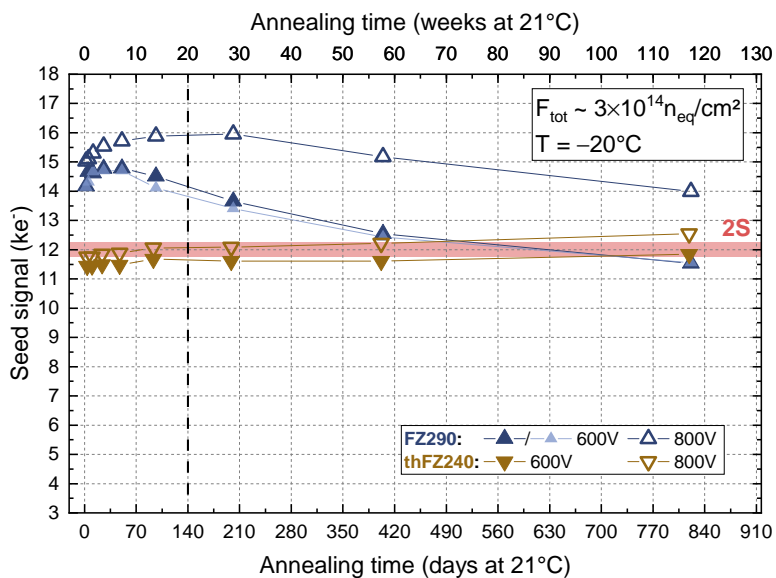
(a) *Maximum* fluence for 2S modules
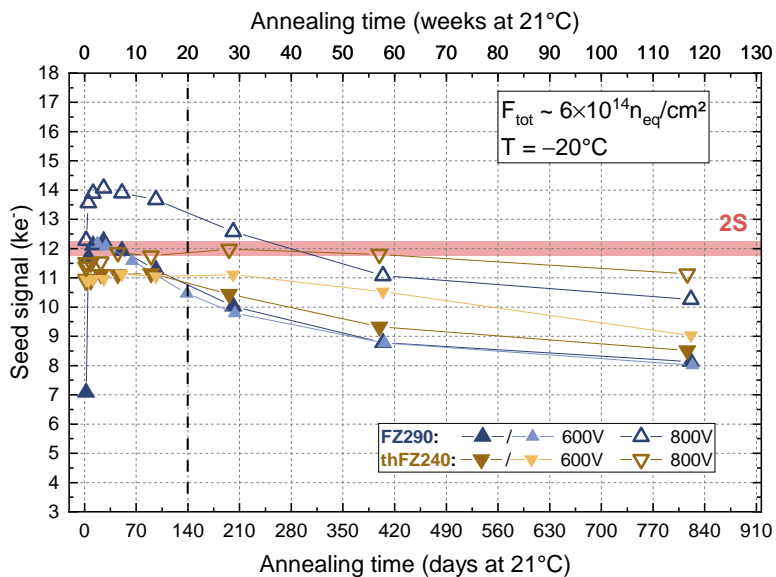
(b) *Ultimate* fluence for 2S modules

Figure 16. Seed signal of FZ290 (upward pointing triangles) and thFZ240 (downward pointing triangles) sensors as a function of equivalent annealing time. The sensors were irradiated to two fluences expected in the tracker region where 2S modules will be installed (or intermediate fluences for the PS region). The symbols with lighter colors are from an additional sensor exposed to the same fluence. Measurements are performed at −20 °C. The horizontal band indicates the envisaged lower signal MPV limit for the given sensor type. The width of the horizontal band is arbitrary. The vertical dashed line indicates the expected annealing time after ten years of operation.

Table 12. The Phase-2 Outer Tracker readout chips and their expected noise (σ) at room temperature [4]. The 4σ-threshold represents the readout threshold. The 12σ-limit represents a conservative estimation of the minimum MPV of the signal height distribution required in order to meet a hit efficiency of at least 99.5% for each readout channel in the future tracker.

Chip	Sensor	σ (e^-)	4σ-threshold (e^-)	12σ-limit (e^-)
CBC	2S	1000	4000	12 000
SSA	PS-s	800	3200	9600
MPA	PS-p	250	1000	3000

on the 2S region. At the fluence of $3 \times 10^{14} \, \mathrm{n_{eq}/cm^2}$ the FZ290 material provides more signal than the thFZ240 material over a wide range of annealing time. The thFZ240 material hardly reaches the required limit. At the *ultimate* fluence of $6 \times 10^{14} \, \mathrm{n_{eq}/cm^2}$ (after $4000 \, \mathrm{fb^{-1}}$ about 1.5% of the 2S modules exceed $5 \times 10^{14} \, \mathrm{n_{eq}/cm^2}$) an increase of the bias voltage to 800 V is required for the FZ290 sensors to satisfy the MPV = $12\,000 \, e^-$ requirement. This increase in bias voltage is not effective for the thin material in the most relevant annealing range (less than 30 weeks at room temperature). An increase of the operation voltage at the end of the HL-LHC run-time in order to maintain efficient operation is an option for the modules that will be exposed to the highest fluences. The power system, module design, and quality control of modules and sensors will all be consistent with an assumed maximum operation voltage of 800 V. The FZ290 sensors are, therefore, well suited for the 2S region of the Phase-2 Outer Tracker and their signal-to-noise performance is better than that of the thFZ240 sensors in the most relevant annealing range.

The plots also include measurements of additional sensors irradiated to the same fluence. Overall they confirm the measurements very well. One exception is shown in figure 16(b) for the thFZ240 material. Here we observed a deviation from the twin measurement, but the height of the initial plateau and the drop at longer annealing times is confirmed. The sensor of the initial (dark) measurements exhibits a higher current and also a soft breakdown during the annealing procedure, which results in a lower signal and also indicates different treatments or damage in this case.

The observations for the PS region are similar (figure 17). The signal in the FZ290 sensors biased at 600 V is larger than the lower limit of $9600 \, e^-$ required for PS-s sensors. Increasing the bias voltage to 800 V ensures a large enough signal of about $10\,500 \, e^-$ even for the maximum fluences expected after $4000 \, \mathrm{fb^{-1}}$ (shown in figure 5). The measured signals of thFZ240 sensors for nominal PS fluences are sufficient at 600 V. At the *ultimate* PS fluence an increase of the bias voltage to 800 V is more effective at higher annealing times, but is not sufficient to raise the signal well above the lower signal limit.

The signal values obtained from FZ290 and thFZ240 sensors at 600 V and 800 V for different fluences have been interpolated to an annealing time of 20 weeks at room temperature and the result of the interpolation is summarized in figure 18. Sensors made of thFZ240 silicon can barely reach the efficient operation region for 2S modules, while FZ290 sensors show high signals. Only beyond $1.5 \times 10^{15} \, \mathrm{n_{eq}/cm^2}$ one can expect benefits from the use of thinner sensors. The lines also indicate a less severe drop of the signal height of FZ290 sensors when exposed to the particle mixture of the
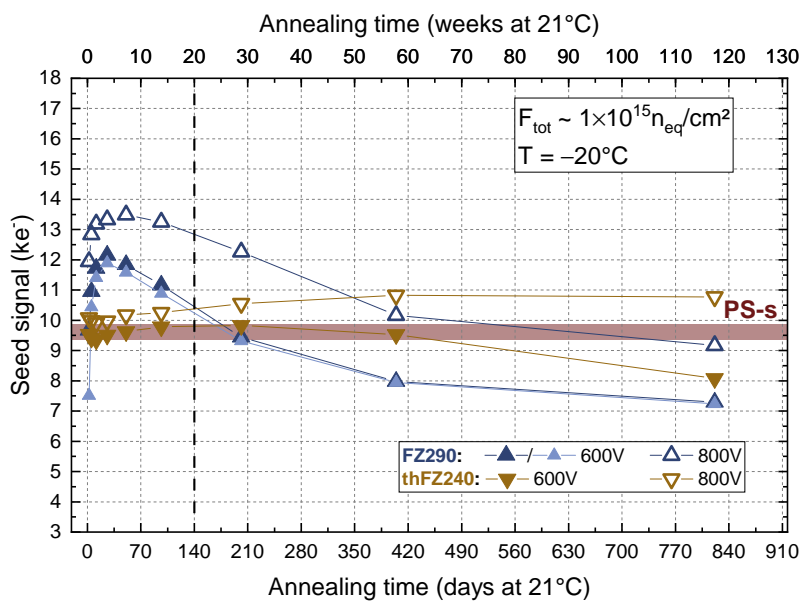
(a) *Maximum* fluence for PS modules
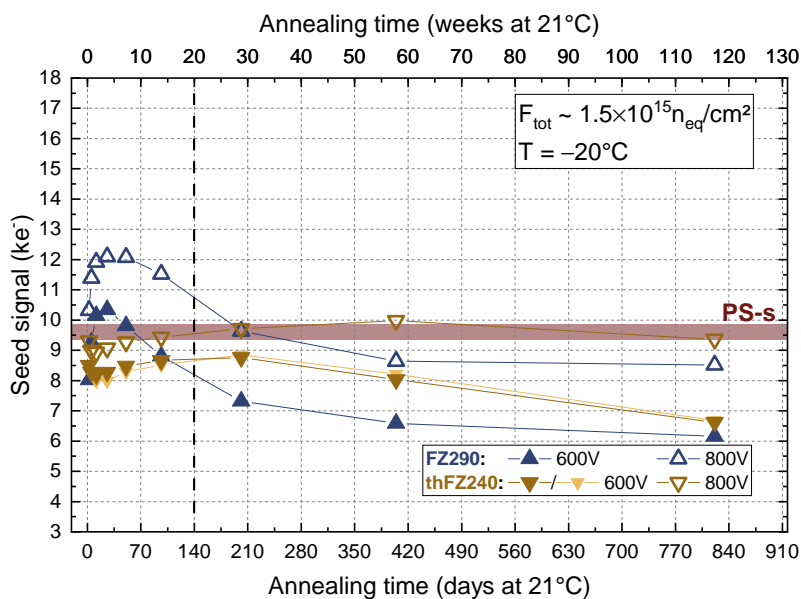
(b) *Ultimate* fluence for PS modules

Figure 17. Seed signal of FZ290 (upward pointing triangles) and thFZ240 (downward pointing triangles) sensors as a function of equivalent annealing time. The sensors were irradiated to two fluences expected in the tracker region where PS modules will be installed. The symbols with lighter colors are from an additional sensor exposed to the same fluence. Measurements are performed at −20 °C. The horizontal band indicates the envisaged lower signal MPV limit for the given sensor type. The width of the horizontal band is arbitrary. The vertical dashed line indicates the expected annealing time after ten years of operation.
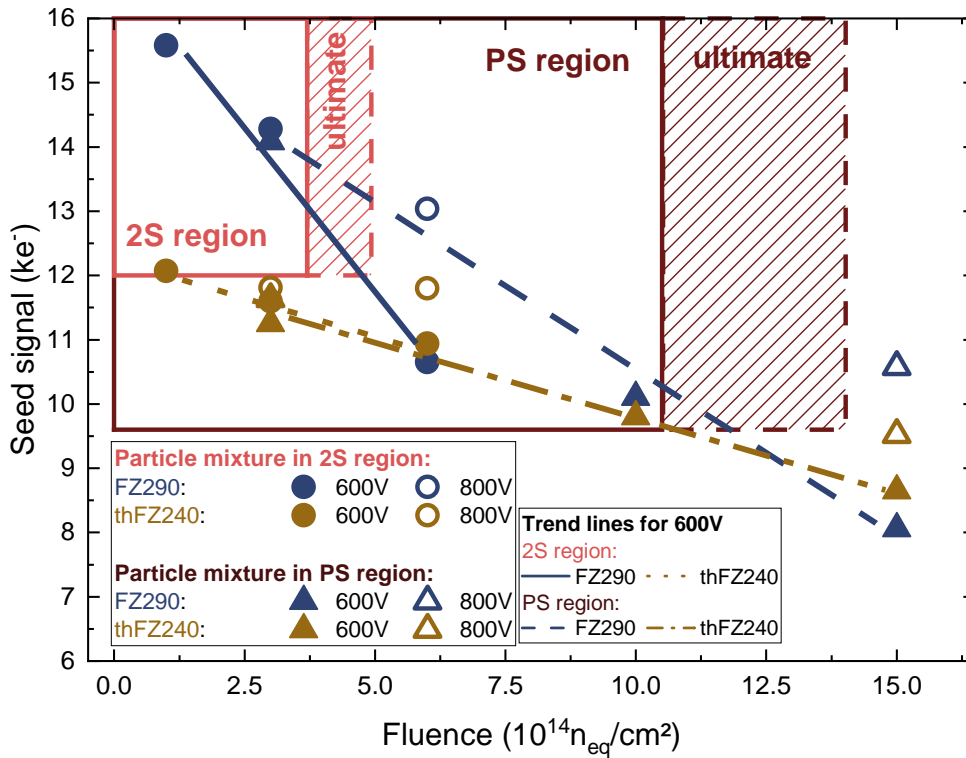
Figure 18. Seed signal of FZ290 (blue) and thFZ240 (brown) sensors for different fluences, measured at a temperature of $-20\,°C$, interpolated to an equivalent annealing of 20 weeks at room temperature. Areas are indicated that represent the signal range required for strip sensors in the 2S and PS region. The solid markers represent measurements conducted at 600 V. Measurement results conducted at 800 V are added in case the initially measured signal is below its specification in order to show the impact of increased bias voltage. The trend of the signals at 600 V for both materials are indicated by the lines.

inner region, which contains a higher fraction of protons. This is consistent with the beneficial effect of higher oxygen content in the bulk reported in literature [13].

The comparison of thinned and thick material was performed with protons of similar energy but from two different sources. We performed additional mixed irradiations with protons from KAZ (after this facility was operational again) and neutrons from JSI to confirm the earlier measurements. The measurement results are shown in figure 19. For the 2S region one can hardly see a difference in the collected seed charge of the thin sensors irradiated with protons at the two facilities and therefore one would also not expect a difference in efficiency. For the higher fluence in the PS region the thin sensors irradiated with the protons at KAZ show a slightly higher signal in the initial ten weeks of annealing, while at longer annealing times the seed signal drops faster than the ones from MC40. The uncertainty in the stated fluences can be up to 15% and might affect the results here. However, the observed signal levels of the thin sensors irradiated at KAZ and MC40 do not deviate more than about 15% at the same annealing time, and the general conclusions on the comparison to the thick sensors are not affected.
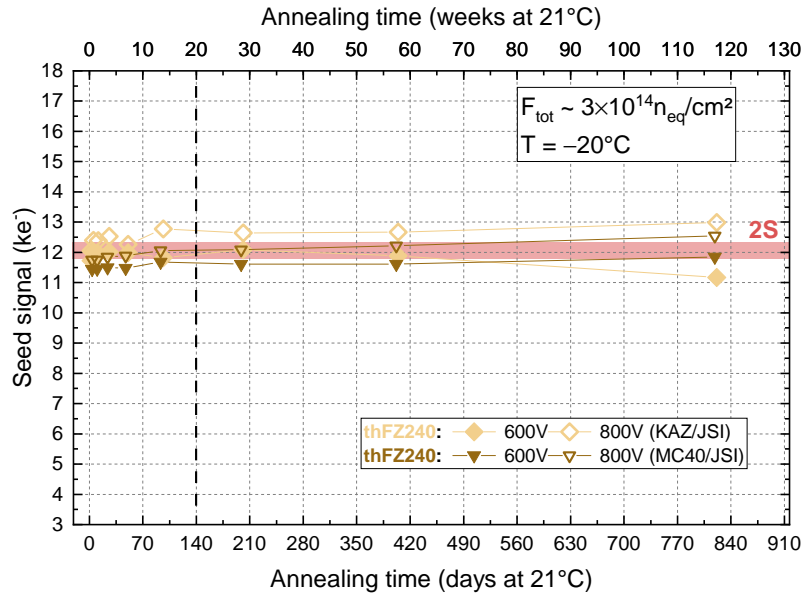
(a) Maximum fluence for 2S modules
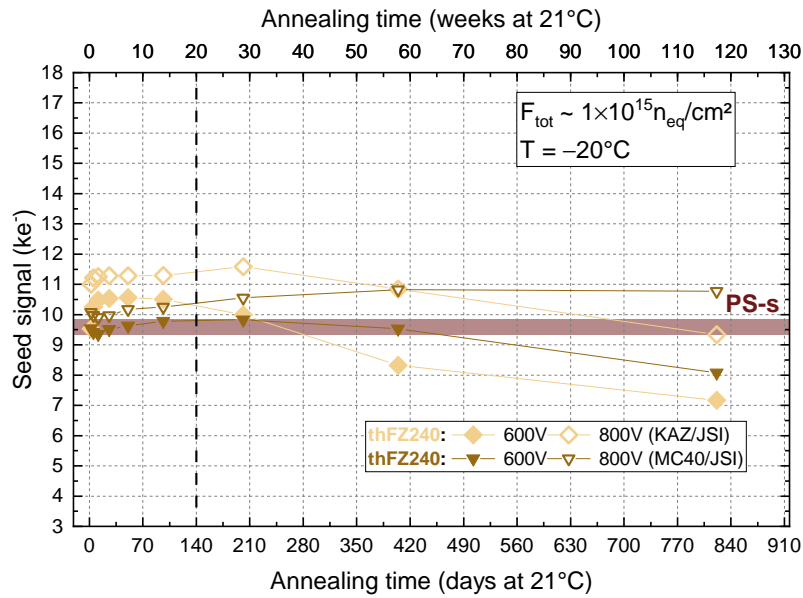
(b) Maximum fluence for PS modules

Figure 19. Seed signal of thin sensors irradiated with neutrons and protons from MC40 (downward pointing triangles) or KAZ (diamonds) as a function of equivalent annealing time. Measurements are performed at $-20\,°C$. The horizontal band indicates the envisaged lower signal limit for the given sensor type. The width of the horizontal band is arbitrary. The vertical dashed line indicates the nominally expected annealing time after ten years of operation.

In conclusion, the FZ290 sensors provide sufficient signal over the course of the nominal HL-LHC period for both the 2S and the PS region. The signal is also sufficient for the expected *ultimate* fluences (corresponding to 4000 fb^{-1}), if the bias voltage is increased up to 800 V. The thFZ240 sensors barely reach the minimum signal for the 2S region for annealing times up to 30 weeks, while they show sufficient signal for the PS region up to 3000 fb^{-1}. However, a small loss in efficiency for both sensor thicknesses at the end of a potential 4000 fb^{-1} scenario of the HL-LHC (corresponding to an ultimate fluence of 1.4×10^{15} n$_{eq}$/cm^2 for few modules) is likely for about 60 modules in the PS region in case the integrated annealing times exceed 30 weeks.

7 Beam test results

For the operation in the CMS tracker the 2S modules are required to have a hit efficiency of 99.5% or better. In addition, the noise hit occupancy must be below 10^{-4}, which is much lower than the expected particle hit occupancy of about 10^{-2}.

At the DESY test beam facility (section 4.3) the hit efficiencies and noise occupancies were measured for normally incident particles for different operating conditions. One parameter that was varied is the global comparator threshold set in the CBCs. For very low thresholds it is expected to record hits generated by noise. For high thresholds the hit detection efficiency drops because of the limited amplitude of the sensor signals. Figure 20 displays the threshold scans for sensors of the two thicknesses irradiated with a fluence of 2.5×10^{14} n$_{eq}$/cm^2. Both sensor thicknesses fulfill the constraints on efficiency and noise hit occupancy in a comfortable threshold range between $3300\,e^-$ and $5500\,e^-$, which allows a flexible selection of the threshold during operation. This reflects the situation for 70% of the 2S modules in the Outer Tracker after 3000 fb^{-1}. Sensors of both thicknesses show very similar properties in this threshold range. The FZ290 material is efficient up to $7000\,e^-$. A stronger dependence on the annealing time can be seen for the FZ290 material compared to the thFZ240 material at 600 V, which was already observed in the laboratory studies illustrated in figure 16.

The results after 5×10^{14} n$_{eq}$/cm^2 are shown in figure 21. This reflects the situation of the most exposed 2S modules in the Outer Tracker after 4000 fb^{-1}. Here the threshold range that satisfies the specifications is small, irrespective of the sensor thickness. The threshold should be at least $3300\,e^-$ to avoid noise hits after long annealing. It is remarkable that the noise occupancy is very similar to the situation after 2.5×10^{14} n$_{eq}$/cm^2 and reflects the very small dependance of the chip noise on leakage current. At the measurement point with a threshold of $4210\,e^-$ the hit efficiencies range from 99.2% to 99.8% depending on the annealing stage. This is just below the requirements for optimal operation. Such high fluences are only expected for about 1.5% of the 2S modules after the extended HL-LHC operation. However, for modules that become inefficient the bias voltage could be increased up to 800 V. Figure 22 shows this effect for both thicknesses after a long annealing time. Sensors of both materials show an efficiency above 99.5% at 800 V for tracks with normal incidence after long and short annealing periods. Signal measurements on these sensors were performed with the ALiBaVa setup described in section 4.2 before assembly of the modules. The measured seed signal is also plotted in figure 22 for comparison. The curves cross the $12\,000\,e^-$ criterion at about the same bias voltages as the efficiency crosses the 99.5% limit and therefore this justifies the initially estimated requirement (section 6).
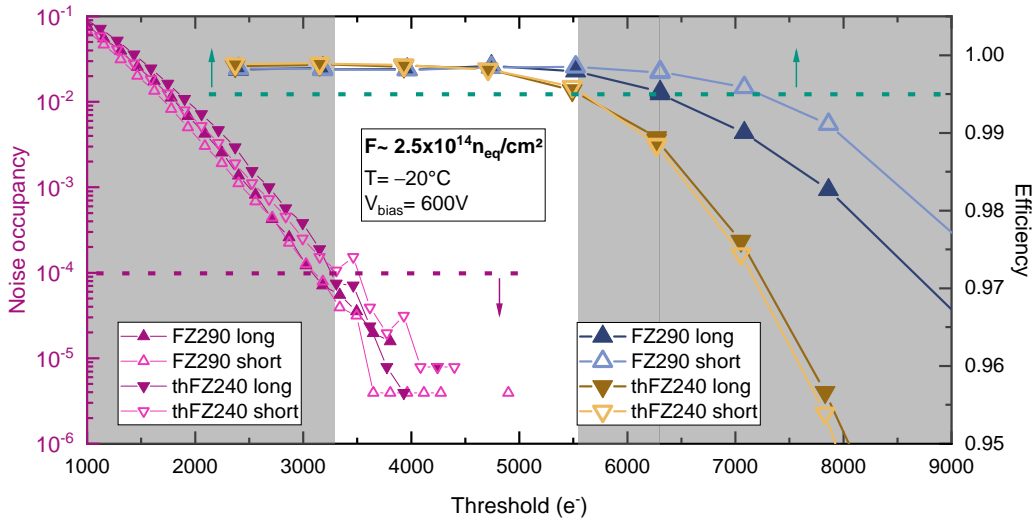
Figure 20. Hit efficiency (blue and brown, right *y*-axis) and noise occupancy (magenta, left *y*-axis) versus threshold for MiMo2. The sensors were irradiated to 2.5×10^{14} n_{eq}/cm^2 and operated at 600 V and $-20\,°C$. The terms "short" (equivalent to 13 days at $+21\,°C$ including 4 days of assembly) and "long" (equivalent to 203 days at $+21\,°C$ including 4 days of assembly) refer to annealing steps performed prior to the measurements. The horizontal dashed lines indicate the specifications for efficiency (green) and noise occupancy (magenta). The gray background indicates the threshold range in which the efficiency and noise requirements are not met by any of the samples with long annealing times. The chip internal DAC value for the comparator threshold was converted to electrons using the relation $1\,V_{Cth} = 156\,e^-$ derived from a testpulse calibration.

So far the presented results were for normal incidence while particles with high transverse momentum (larger than $2\,GeV/c$) in the experiment also pass the sensors at angles up to about $18°$ [4]. To study efficiency and cluster size for different particle incidence angles the modules were rotated in the beam. Figure 23 shows these two quantities as a function of the inclination angle. The cluster size in number of channels increases continuously from 1.15 at $0°$ to just below 2 at $40°$. The efficiency increases until a maximum is reached at about 10 to $20°$ and then drops slightly towards the highest angle measured. The effect on the efficiency is less than 1% and similar for the two thicknesses.

8 Further considerations

There are additional considerations that enter into the choice of sensor thickness, namely cost, robustness, and material budget.

The additional thinning step implies additional costs, which has a big impact considering that 24 000 wafers will be required for the Phase-2 Outer Tracker.

The backside of the thinned sensors is processed differently, leading to a quite shallow doping layer. This makes thinned sensors more prone to scratch-induced early IV breakdowns, i.e., sharp or exponential current increase at bias voltages below 600 V. This was confirmed during the measurements of the 60 full-size sensors that were characterized in parallel to the irradiation
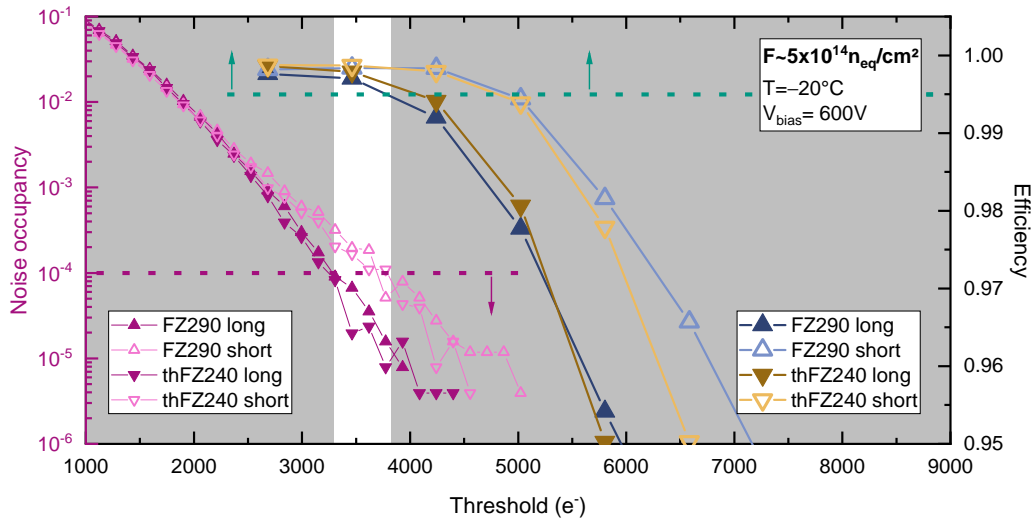
Figure 21. Hit efficiency (blue and brown, right *y*-axis) and noise occupancy (magenta, left *y*-axis) versus threshold for MiMo3. The sensors were irradiated to 5×10^{14} n_{eq}/cm^2 and operated at 600 V and $-20\,°C$. The terms "short" (equivalent to 13 days at $+21\,°C$ including 4 days of assembly) and "long" (equivalent to 203 days at $21\,°C$ including 4 days of assembly) refer to annealing steps performed prior to the measurements. The horizontal dashed lines indicate the specifications for efficiency (green) and noise occupancy (magenta). The gray background indicates the threshold range in which the efficiency and noise requirements are not met by any of the samples with long annealing times. The chip internal DAC value for the comparator threshold was converted to electrons using the relation $1\,V_{Cth} = 156\,e^-$ derived from a testpulse calibration.
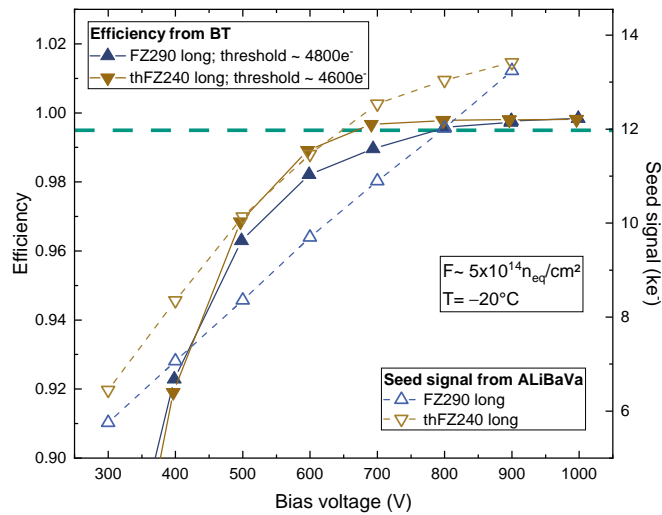

Figure 22. Hit efficiency (left axis) and seed signal (right axis) versus bias voltage for the sensors on MiMo3 irradiated to a fluence of 5.0×10^{14} n_{eq}/cm^2 and 203 days equivalent annealing at $+21\,°C$. The module was operated at $-20\,°C$ and at a threshold of about $4800\,e^-/4600\,e^-$ in the beam test (BT). By increasing the bias voltage to 800 V the efficiency reaches the 99.5% criterion. This correlates with the bias voltage dependence of the seed signal measured in the ALiBaVa system before assembly, and motivates the $12\,000\,e^-$ criterion set before.
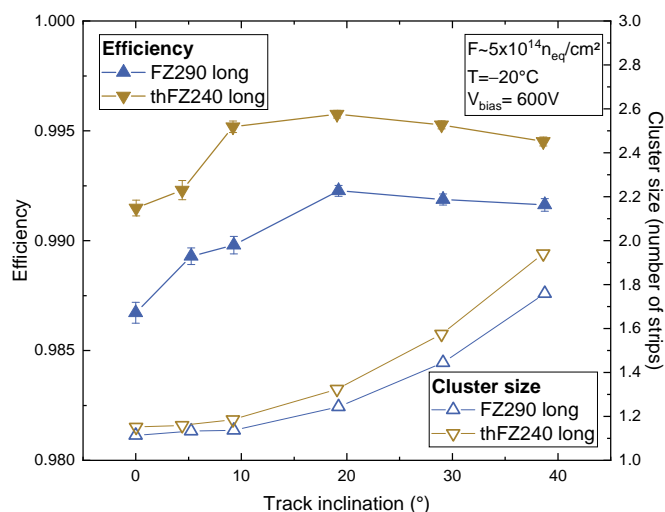
Figure 23. Efficiency (left axis) and cluster size (right axis) versus the inclination angle of the incident particles for the sensors on MiMo3 irradiated to a fluence of 5.0×10^{14} n_{eq}/cm^2 and 203 days equivalent annealing at +21 °C. The module was operated at −20 °C and at a threshold of about 3450 e^- in the beam test.

campaign. Figure 24 shows the leakage currents of full-size 2S sensors at a bias voltage of 400 V. The different bars represent different measurements at the same or different sites, as indicated in the legend. Currents exceeding 1000 nA or large variations between measurements after normal handling are considered suspicious and are indications of reduced breakdown voltage. It is obvious that many more of the thFZ240 sensors are affected. This is a critical issue, which could lead to severe problems during the mass production of Outer Tracker modules.

One of the benefits of thinner silicon sensors is a reduction of the material budget. Compared to the 320 μm thick sensors the 240 μm thick ones have 25% less mass. When looking at the total module mass of about 30 g, though, the benefit of using thFZ240 material is reduced to a mass saving of 10% only. Furthermore, the material amount crossed by straight tracks in units of radiation and interaction lengths in the tracking volume of the Phase-2 Outer Tracker with FZ290 or thFZ240 sensors was computed by a fast simulation (tkLayout [36, 37]), considering the detector material up to the last active hit. The results are shown in table 13. The thicker sensors only add about 1.6% of a radiation length to the entire tracking volume. Moreover, modules with thin sensors might require additional material to remove the heat from the sensors, while for the thick sensors the additional silicon acts as a heat spreader. This aspect would further reduce the difference in the number of radiation lengths between FZ290 and thFZ240 sensors. This small reduction of the material budget for the thin sensors would only be exploited if the performance was identical for both materials.

9 Conclusion

The CMS Collaboration performed a direct comparison of the baseline FZ290 and thinned (240 μm thick) thFZ240 silicon strip sensors from HPK in view of their performance over the lifetime of the experiment. Characterization of the strip parameters did not reveal any significant issues with either of the materials.
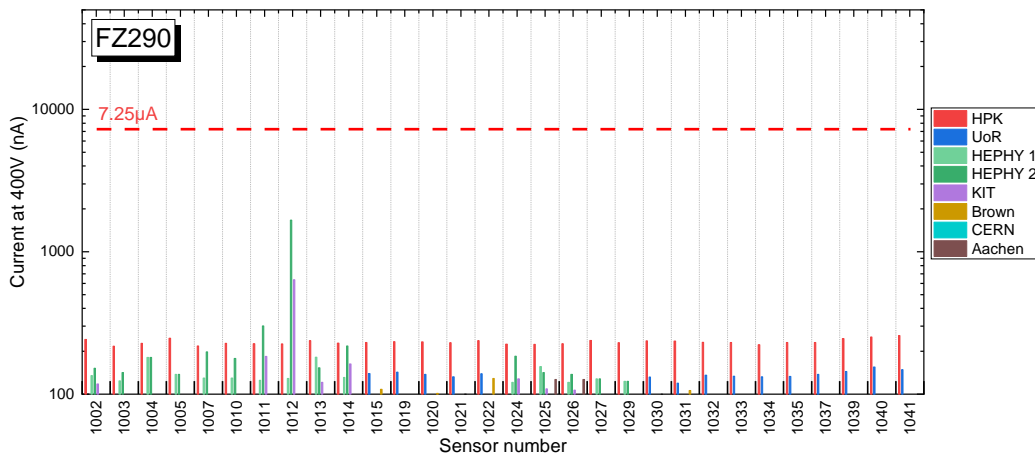
(a) Full-size 2S sensors of FZ290 type
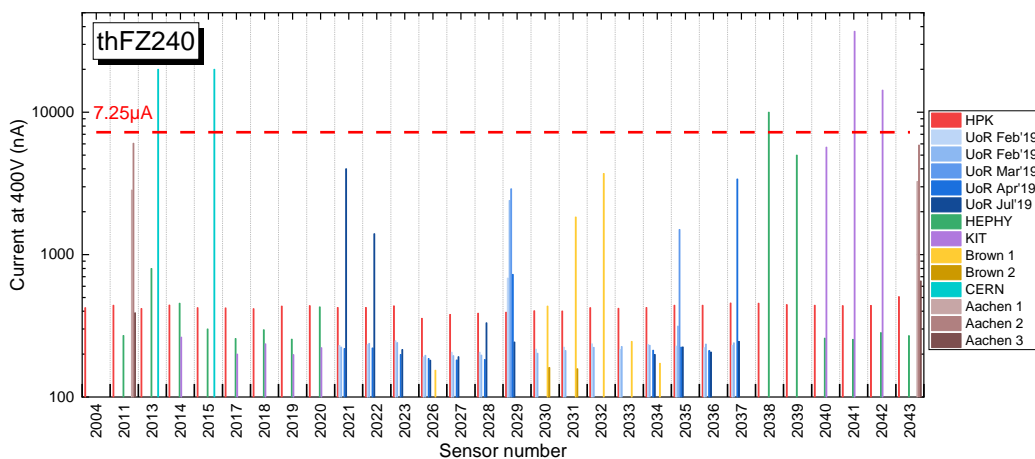
(b) Full-size 2S sensors of thFZ240 type

Figure 24. Leakage current of full-size 2S sensors measured at a bias voltage of 400 V at room temperature. The different bars represent different measurements at the same or at different sites as indicated in the legend: vendor test at HPK (HPK); sensor quality control at University of Rochester (UoR), Institute of High Energy Physics in Vienna (HEPHY), Karlsruhe Institute of Technology (KIT), and Brown University (Brown); reception test before module assembly at RWTH Aachen (Aachen) and CERN (CERN). The horizontal red line indicates the specification for the maximum current. The vendor test was performed at about 5 °C higher temperature, which would tend to result in higher currents.

Table 13. Calculated average fractions of radiation (X/X_0) and interaction (λ/λ_0) length in the tracking volume for the Outer Tracker and the entire tracking system including the inner pixel detector and services. Calculations were performed with tkLayout using layout version OT801_IT701 [38]. The relative difference is defined as: $(P_{\mathrm{FZ290}} - P_{\mathrm{thFZ240}})/P_{\mathrm{thFZ240}}$, where P stands for the respective fractions of radiation or interaction lengths.

Sensor material	Outer Tracker		Entire Tracker	
	X/X_0	λ/λ_0	X/X_0	λ/λ_0
FZ290	20.5%	6.21%	56.1%	17.94%
thFZ240	19.6%	6.02%	55.2%	17.76%
Relative difference	4.6%	3.2%	1.6%	1.0%

After irradiation with a mixture of protons and neutrons up to fluences expected in the CMS tracker after $4000\,\mathrm{fb}^{-1}$ the collected seed charge was measured as a function of the annealing time (section 6). These results showed that the thicker FZ290 sensors provide a higher signal for most of the parameter space in terms of fluence and annealing time. Only at fluences above $1 \times 10^{15}\,\mathrm{n_{eq}/cm^2}$ and annealing times beyond 30 weeks thinned thFZ240 sensors provide higher signals. In this specific case, the FZ290 sensors can still reach the estimated minimum signal for high efficiency by increasing the bias voltage from the nominal 600 V to 800 V.

Finally, the irradiated sensors were compared in a beam test at DESY, where both sensor types showed hit efficiencies above 99.5 % for the expected fluence scenarios in the 2S region (section 7).

In conclusion, sensors of both thicknesses could be used in the CMS tracker at HL-LHC, while the FZ290 sensors provide improved longevity by delivering a higher signal compared to the thinned material for most positions in the tracker. In extreme cases, the thFZ240 material would provide a slightly higher signal at nominal voltage, but these signal levels could also be obtained for FZ290 sensor modules by applying a higher bias voltage.

Since both sensor thicknesses fulfill the minimum performance requirements, further considerations about longevity, handling (thinned sensors are more prone to scratch-induced early IV breakdowns), and costs led the CMS Collaboration to choose the FZ290 sensors.

References

[1] The High Luminosity LHC Project, https://hilumilhc.web.cern.ch/.

[2] I. Bejar Alonso and L. Rossi, *HiLumi LHC Technical Design Report: Deliverable: D1.10*, Tech. Rep., CERN-ACC-2015-0140 (2015).

[3] CMS collaboration, *The CMS Experiment at the CERN LHC*, 2008 *JINST* **3** S08004.

[4] CMS collaboration, *The Phase-2 Upgrade of the CMS Tracker*, Tech. Rep., CERN-LHCC-2017-009, CMS-TDR-014, CERN, Geneva (2017).

[5] G. Hall et al., *CBC2: A CMS microstrip readout ASIC with logic for track-trigger modules at HL-LHC*, *Nucl. Instrum. Meth. A* **765** (2014) 214.

[6] K. Uchida et al., *Results from the CBC3 readout ASIC for CMS 2S-modules*, *Nucl. Instrum. Meth. A* **924** (2019) 175.

[7] A. Caratelli et al., *Characterization of the first prototype of the Silicon-Strip readout ASIC (SSA) for the CMS Outer-Tracker phase-2 upgrade*, *PoS* **TWEPP2018** (2019) 159.

[8] D. Ceresa et al., *Characterization of the MPA prototype, a 65 nm pixel readout ASIC with on-chip quick transverse momentum discrimination capabilities*, *PoS* **TWEPP2018** (2019) 166.

[9] A. La Rosa, *The CMS Outer Tracker for the High Luminosity LHC upgrade*, 2020 *JINST* **15** C02029 [arXiv:1912.02061].

[10] The TRACKER GROUP of the CMS collaboration, *P-Type Silicon Strip Sensors for the new CMS Tracker at HL-LHC*, 2017 *JINST* **12** P06018.

[11] The TRACKER GROUP of the CMS collaboration, *Experimental study of different silicon sensor options for the upgrade of the CMS Outer Tracker*, 2020 *JINST* **15** P04017 [arXiv:2001.02023].

[12] F. Hartmann, *Evolution of Silicon Sensor Technology in Particle Physics*, Springer Tracts in Modern Physics, vol. 274, second edition, ISBN 978-3-319-64434-9.

[13] M. Huhtinen, *Simulation of non-ionising energy loss and defect formation in silicon*, *Nucl. Instrum. Meth. A* **491** (2002) 194.

[14] Particle transport simulation FLUKA, https://fluka.cern.

[15] G. Battistoni et al., *Overview of the FLUKA code*, *Ann. Nucl. Energy* **82** (2015) 10.

[16] CMS collaboration, *1-D plot covering CMS tracker, showing FLUKA simulated 1 MeV neutron equivalent in Silicon including contributions from various particle types*, CMS-DP-2015-022. .

[17] Karlsruhe Irradiation Center, https://www.etp.kit.edu/english/irradiation_center.php.

[18] P. Allport et al., *Recent results and experience with the Birmingham MC40 irradiation facility*, 2017 *JINST* **12** C03075.

[19] L. Snoj, G. Žerovnik and A. Trkov, *Computational analysis of irradiation facilities at the JSI TRIGA reactor*, *Appl. Radiat. Isot.* **70** (2012) 483.

[20] D. Zontar, V. Cindro, G. Kramberger and M. Mikuz, *Time development and flux dependence of neutron-irradiation induced defects in silicon pad detectors*, *Nucl. Instrum. Meth. A* **426** (1999) 51.

[21] Rhode Island Nuclear Science Center, http://www.rinsc.ri.gov/.

[22] S. Seif El Nasr-Storey, *Recent developments in the CBC3, a CMS micro-strip readout ASIC for track-trigger modules at the HL-LHC*, *Nucl. Instrum. Meth. A* **936** (2019) 278.

[23] R. Marco-Hernández, *A portable readout system for silicon microstrip sensors*, *Nucl. Instrum. Meth. A* **623** (2010) 207.

[24] ALiBaVa Systems, http://www.alibavasystems.com.

[25] S. Löchner and M. Schmelling, The Beetle Reference Manual for Beetle version 1.3/1.4/1.5, LHCb-2005-105. http://www.kip.uni-heidelberg.de/lhcb/Publications/BeetleRefMan_v1_3.pdf.

[26] M. Moll, *Radiation Damage in Silicon Particle Detectors*, Ph.D. thesis, University of Hamburg (1999) [DESY-THESIS-1999-040].

[27] M. Metzler, *Irradiation studies on n-in-p silicon strip sensors in the course of the CMS Phase-2 Outer Tracker Upgrade*, Ph.D. thesis, Karlsruhe Institute of Technology (2020) [ETP-KA/2020-2].

[28] R. Frühwirth, H. Pernegger and M. Friedl, *Convoluted Landau and Gaussian Fitting Function (using ROOT's Landau and Gauss functions)*, https://root.cern.ch/root/html404/examples/langaus.C.html

[29] R. Diener et al., *The DESY II Test Beam Facility*, *Nucl. Instrum. Meth. A* **922** (2019) 265 [arXiv:1807.09328].

[30] H. Jansen et al., *Performance of the EUDET-type beam telescopes*, *EPJ Techn. Instrum.* **3** (2016) 1.

[31] C. Hu-Guo et al., *First reticle size MAPS with digital output and integrated zero suppression for the EUDET-JRA1 beam telescope*, *Nucl. Instrum. Meth. A* **623** (2010) 480.

[32] H. Perrey, *EUDAQ and EUTelescope: Software Frameworks for Test Beam Data Acquisition and Analysis*, *PoS* **TIPP2014** (2014) 353.

[33] A. Bulgheroni et al., *EUTelescope: tracking software*, EUDET-Memo-2007-20 (2007).

[34] A. Chilingarov, *Temperature dependence of the current generated in Si bulk*, 2013 *JINST* **8** P10003.

[35] K.-H. Hoffmann, *Development of new Sensor Designs and Investigations on Radiation Hard Silicon Strip Sensors for the CMS Tracker Upgrade at the High Luminosity Large Hadron Collider*, Ph.D. thesis, Karlsruhe Institute of Technology (2013) IEKP-KA/2013-1.

[36] CMS collaboration, *tkLayout: a design tool for innovative silicon tracking detectors*, 2014 *JINST* **9** C03054.

[37] tkLayout web site, https://tklayout.web.cern.ch/.

[38] Version OT801_IT701 of the CMS Phase-2 TK Layout, https://cms-tklayout.web.cern.ch/cms-tklayout/layouts-work/recent-layouts/OT801_IT701/index.html.

The Tracker Group of the CMS Collaboration

Institut für Hochenergiephysik, Wien, Austria

W. Adam, T. Bergauer, D. Blöch, M. Dragicevic, R. Frühwirth[1], V. Hinger, H. Steininger

Universiteit Antwerpen, Antwerpen, Belgium

W. Beaumont, D. Di Croce, X. Janssen, T. Kello, A. Lelek, P. Van Mechelen, S. Van Putte, N. Van Remortel

Vrije Universiteit Brussel, Brussel, Belgium

F. Blekman, M. Delcourt, J. D'Hondt, S. Lowette, S. Moortgat, A. Morton, D. Muller, A.R. Sahasransu, E. Sørensen Bols

Université Libre de Bruxelles, Bruxelles, Belgium

Y. Allard, D. Beghin, B. Bilin, B. Clerbaux, G. De Lentdecker, W. Deng, L. Favart, A. Grebenyuk, D. Hohov, A. Kalsi, A. Khalilzadeh, M. Mahdavikhorrami, I. Makarenko, L. Moureaux, A. Popov, N. Postiau, F. Robert, Z. Song, L. Thomas, P. Vanlaer, D. Vannerom, Q. Wang, H. Wang, Y. Yang

Université Catholique de Louvain, Louvain-la-Neuve, Belgium

A. Bethani, G. Bruno, F. Bury, C. Caputo, P. David, A. Deblaere, C. Delaere, I.S. Donertas, A. Giammanco, V. Lemaitre, K. Mondal, J. Prisciandaro, N. Szilasi, A. Taliercio, M. Teklishyn, P. Vischia, S. Wertz

Institut Ruđer Bošković, Zagreb, Croatia

V. Brigljević, D. Ferenček, D. Majumder, S. Mishra, M. Roguljić, A. Starodumov[2], T. Šuša

Department of Physics, University of Helsinki, Helsinki, Finland

P. Eerola

Helsinki Institute of Physics, Helsinki, Finland

E. Brücken, T. Lampén, L. Martikainen, E. Tuominen

Lappeenranta-Lahti University of Technology, Lappeenranta, Finland

P. Luukka, T. Tuuva

Université de Strasbourg, CNRS, IPHC UMR 7178, Strasbourg, France

J.-L. Agram[3], J. Andrea, D. Apparu, D. Bloch, C. Bonnin, G. Bourgatte, J.-M. Brom, E. Chabert, L. Charles, C. Collard, E. Dangelser, D. Darej, U. Goerlach, C. Grimault, L. Gross, C. Haas, M. Krauth, E. Nibigira, N. Ollivier-Henry, E. Silva Jiménez

Université de Lyon, Université Claude Bernard Lyon 1, CNRS/IN2P3, IP2I Lyon, UMR 5822, Villeurbanne, France

E. Asilar, G. Baulieu, G. Boudoul, L. Caponetto, N. Chanon, D. Contardo, P. Dené, T. Dupasquier, G. Galbit, S. Jain, N. Lumb, L. Mirabito, B. Nodari, S. Perries, M. Vander Donckt, S. Viret

RWTH Aachen University, I. Physikalisches Institut, Aachen, Germany

V. Botta, L. Feld, W. Karpinski, K. Klein, M. Lipinski, D. Louis, D. Meuser, A. Pauls, G. Pierschel, M. Rauch, N. Röwert, J. Schulz, M. Teroerde, M. Wlochal

RWTH Aachen University, III. Physikalisches Institut B, Aachen, Germany

C. Dziwok, G. Fluegge, O. Pooth, A. Stahl, T. Ziemons

Deutsches Elektronen-Synchrotron, Hamburg, Germany

C. Cheng, P. Connor, A. De Wit, G. Eckerlin, D. Eckstein, E. Gallo, M. Guthoff, A. Harb, C. Kleinwort, R. Mankel, H. Maser, M. Meyer, C. Muhl, A. Mussgiller, Y. Otarid, D. Pitzl, O. Reichelt, M. Savitskyi, R. Stever, N. Tonon, A. Velyka, R. Walsh, Q. Wang, A. Zuber

Institut für Experimentelle Teilchenphysik, KIT, Karlsruhe, Germany

M. Abbas, L. Ardila[4], M. Balzer[4], T. Barvich, T. Blank[4], E. Butz, M. Caselle[4], W. De Boer[†], A. Dierlamm[4], A. Droll, U. Elicabuk, K. El Morabit[5], F. Hartmann, U. Husemann, R. Koppenhöfer, S. Maier, S. Mallows, T. Mehner[4], M. Metzler, J. Modes, J.-O. Müller-Gosewisch, Th. Muller, M. Neufeld, A. Nürnberg[6], O. Sander[4], D. Schell, M. Schröder[5], I. Shvetsov, H.J. Simonis, J. Stanulla, P. Steck, M. Wassmer, M. Weber[4], A. Weddigen, F. Wittig

Institute of Nuclear and Particle Physics (INPP), NCSR Demokritos, Aghia Paraskevi, Greece

G. Anagnostou, P. Assiouras, G. Daskalakis, I. Kazas, A. Kyriakis, D. Loukas

Wigner Research Centre for Physics, Budapest, Hungary

T. Balázs, K. Márton, F. Siklér, V. Veszprémi

National Institute of Science Education and Research, HBNI, Bhubaneswar, India

A. Das, C. Kar, P. Mal, R. Mohanty, P. Saha, S. Swain

University of Delhi, Delhi, India

A. Bhardwaj, C. Jain, G. Jain, A. Kumar, K. Ranjan, S. Saumya

Saha Institute of Nuclear Physics, Kolkata, India

R. Bhattacharya, S. Dutta, P. Palit, G. Saha, S. Sarkar

INFN Sezione di Bari[a], Università di Bari[b], Politecnico di Bari[c], Bari, Italy

P. Cariola[a], D. Creanza[a,c], M. de Palma[a,b], G. De Robertis[a], L. Fiore[a], M. Ince[a,b], F. Loddo[a], G. Maggi[a,c], S. Martiradonna[a], M. Mongelli[a], S. My[a,b], G. Selvaggi[a,b], L. Silvestris[a]

INFN Sezione di Catania[a], Università di Catania[b], Catania, Italy

S. Albergo[a,b], S. Costa[a,b], A. Di Mattia[a], R. Potenza[a,b], M.A. Saizu[a,7], A. Tricomi[a,b], C. Tuve[a,b]

INFN Sezione di Firenze[a], Università di Firenze[b], Firenze, Italy

G. Barbagli[a], M. Brianzi[a], A. Cassese[a], R. Ceccarelli[a,b], R. Ciaranfi[a], V. Ciulli[a,b], C. Civinini[a], R. D'Alessandro[a,b], F. Fiori[a,b], E. Focardi[a,b], G. Latino[a,b], P. Lenzi[a,b], M. Lizzo[a,b], M. Meschini[a], S. Paoletti[a], R. Seidita[a,b], G. Sguazzoni[a], L. Viliani[a]

INFN Sezione di Genova, Genova, Italy

F. Ferro, E. Robutti

INFN Sezione di Milano-Bicocca[a], Università di Milano-Bicocca[b], Milano, Italy

F. Brivio[a], M.E. Dinardo[a,b], P. Dini[a], S. Gennai[a], L. Guzzi[a,b], S. Malvezzi[a], D. Menasce[a], L. Moroni[a], D. Pedrini[a], D. Zuolo[a,b]

INFN Sezione di Padova^a, Università di Padova^b, Padova, Italy

P. Azzi^a, N. Bacchetta^a, P. Bortignon^{a,8}, D. Bisello^a, T. Dorigo^a, M. Tosi^{a,b}, H. Yarar^{a,b}

INFN Sezione di Pavia^a, Università di Bergamo^b, Bergamo, Università di Pavia^c, Pavia, Italy

L. Gaioni^{a,b}, M. Manghisoni^{a,b}, L. Ratti^{a,c}, V. Re^{a,b}, E. Riceputi^{a,b}, G. Traversi^{a,b}

INFN Sezione di Perugia^a, Università di Perugia^b, CNR-IOM Perugia^c, Perugia, Italy

P. Asenov^{a,c}, G. Baldinelli^{a,b}, F. Bianchi^{a,b}, G.M. Bilei^a, S. Bizzaglia^a, M. Caprai^a, B. Checcucci^a, D. Ciangottini^a, L. Fanò^{a,b}, L. Farnesini^a, M. Ionica^a, M. Magherini^{a,b}, G. Mantovani^{a,b}, V. Mariani^{a,b}, M. Menichelli^a, A. Morozzi^a, F. Moscatelli^{a,c}, D. Passeri^{a,b}, A. Piccinelli^{a,b}, P. Placidi^{a,b}, A. Rossi^{a,b}, A. Santocchia^{a,b}, D. Spiga^a, L. Storchi^a, T. Tedeschi^{a,b}, C. Turrioni^{a,b}

INFN Sezione di Pisa^a, Università di Pisa^b, Scuola Normale Superiore di Pisa^c, Pisa, Italy

P. Azzurri^a, G. Bagliesi^a, A. Basti^a, R. Beccherle^a, V. Bertacchi^{a,c}, L. Bianchini^a, T. Boccali^a, F. Bosi^a, R. Castaldi^a, M.A. Ciocci^{a,b}, R. Dell'Orso^a, S. Donato^a, A. Giassi^a, M.T. Grippo^{a,b}, F. Ligabue^{a,c}, G. Magazzu^a, E. Manca^{a,c}, G. Mandorli^{a,c}, M. Massa^a, E. Mazzoni^a, A. Messineo^{a,b}, A. Moggi^a, F. Morsani^a, F. Palla^a, S. Parolia^{a,b}, F. Raffaelli^a, G. Ramirez Sanchez^{a,c}, A. Rizzi^{a,b}, S. Roy Chowdhury^{a,c}, P. Spagnolo^a, R. Tenchini^a, G. Tonelli^{a,b}, A. Venturi^a, P.G. Verdini^a

INFN Sezione di Torino^a, Università di Torino^b, Torino, Italy

R. Bellan^{a,b}, S. Coli^a, M. Costa^{a,b}, R. Covarelli^{a,b}, G. Dellacasa^a, N. Demaria^a, S. Garbolino^a, M. Grippo^{a,b}, E. Migliore^{a,b}, E. Monteil^{a,b}, M. Monteno^a, G. Ortona^a, L. Pacher^{a,b}, A. Rivetti^a, A. Solano^{a,b}, A. Vagnerini^{a,b}

Vilnius University, Vilnius, Lithuania

M. Ambrozas, A. Juodagalvis, A. Rinkevicius

National Centre for Physics, Islamabad, Pakistan

A. Ahmad, S. Muhammad, A. Sultan

Instituto de Física de Cantabria (IFCA), CSIC-Universidad de Cantabria, Santander, Spain

E. Curras Rivera, J. Duarte Campderros, M. Fernandez, A. Garcia Alonso, G. Gomez, F.J. Gonzalez Sanchez, R. Jaramillo Echeverria, D. Moya, A. Ruiz Jimeno, L. Scodellaro, I. Vila, A.L. Virto, J.M. Vizan Garcia

CERN, European Organization for Nuclear Research, Geneva, Switzerland

D. Abbaneo, I. Ahmed, E. Albert, J. Almeida, M. Barinoff, J. Batista Lopes, G. Bergamin[9], G. Blanchot, F. Boyer, A. Caratelli, R. Carnesecchi, D. Ceresa, J. Christiansen, K. Cichy, J. Daguin, S. Detraz, M. Dudek, N. Emriskova[10], F. Faccio, N. Frank, T. French, A. Hollos, G. Hugo, J. Kaplon, Z. Kerekes, K. Kloukinas, N. Koss, L. Kottelat, D. Koukola, M. Kovacs, A. La Rosa, P. Lenoir, R. Loos, A. Marchioro, I. Mateos Dominguez[11], S. Mersi, S. Michelis, A. Millet, A. Onnela, S. Orfanelli, T. Pakulski, A. Papadopoulos[12], A. Perez, F. Perez Gomez, J.-F. Pernot, P. Petagna, Q. Piazza, P. Rose, S. Scarfì[13], M. Sinani, R. Tavares Rego, P. Tropea, J. Troska, A. Tsirou, F. Vasey, P. Vichoudis, A. Zografos[14]

Paul Scherrer Institut, Villigen, Switzerland

W. Bertl[†], L. Caminada[15], A. Ebrahimi, W. Erdmann, R. Horisberger, H.-C. Kaestli, D. Kotlinski, U. Langenegger, B. Meier, M. Missiroli[15], L. Noehte[15], T. Rohe, S. Streuli

Institute for Particle Physics, ETH Zurich, Zurich, Switzerland

K. Androsov, M. Backhaus, R. Becker, P. Berger, A. De Cosa, D. di Calafiori, A. Calandri, L. Djambazov, M. Donega, C. Dorfer, F. Eble, F. Glessgen, C. Grab, D. Hits, W. Lustermann, M. Meinhard, J. Niedziela, V. Perovic, M. Reichmann, B. Ristic, U. Roeser, D. Ruini, J. Sörensen, R. Wallny

Universität Zürich, Zurich, Switzerland

K. Bösiger, D. Brzhechko, F. Canelli, K. Cormier, R. Del Burgo, M. Huwiler, A. Jofrehei, B. Kilminster, S. Leontsinis, A. Macchiolo, U. Molinatti, R. Maier, V. Mikuni, I. Neutelings, A. Reimers, P. Robmann, Y. Takahashi, D. Wolf

National Taiwan University (NTU), Taipei, Taiwan

P.-H. Chen, W.-S. Hou, R.-S. Lu

University of Bristol, Bristol, United Kingdom

E. Clement, D. Cussans, J. Goldstein, S. Seif El Nasr-Storey, N. Stylianou

Rutherford Appleton Laboratory, Didcot, United Kingdom

J.A. Coughlan, K. Harder, K. Manolopoulos, I.R. Tomalin

Imperial College, London, United Kingdom

R. Bainbridge, J. Borg, C. Brown, G. Fedi, G. Hall, D. Monk, M. Pesaresi, K. Uchida

Brunel University, Uxbridge, United Kingdom

K. Coldham, J. Cole, M. Ghorbani, A. Khan, P. Kyberd, I.D. Reid

The Catholic University of America, Washington DC, U.S.A.

R. Bartek, A. Dominguez, R. Uniyal, A.M. Vargas Hernandez

Brown University, Providence, U.S.A.

G. Benelli, B. Burkle, X. Coubez, U. Heintz, N. Hinton, J. Hogan[16], A. Honma, A. Korotkov, D. Li, M. Lukasik, M. Narain, S. Sagir[17], F. Simpson, E. Spencer, E. Usai, J. Voelker, W.Y. Wong, W. Zhang

University of California, Davis, Davis, U.S.A.

E. Cannaert, M. Chertok, J. Conway, G. Haza, D. Hemer, F. Jensen, J. Thomson, W. Wei, T. Welton, R. Yohay[18], F. Zhang

University of California, Riverside, Riverside, U.S.A.

G. Hanson, W. Si

University of California, San Diego, La Jolla, U.S.A.

P. Chang, S.B. Cooperstein, N. Deelen, R. Gerosa, L. Giannini, S. Krutelyov, B.N. Sathia, V. Sharma, M. Tadel, A. Yagil

University of California, Santa Barbara - Department of Physics, Santa Barbara, U.S.A.

V. Dutta, L. Gouskos, J. Incandela, M. Kilpatrick, S. Kyre, H. Qu, M. Quinnan

University of Colorado Boulder, Boulder, U.S.A.

J.P. Cumalat, W.T. Ford, E. MacDonald, A. Perloff, K. Stenson, K.A. Ulmer, S.R. Wagner

Cornell University, Ithaca, U.S.A.

J. Alexander, Y. Bordlemay Padilla, S. Bright-Thonney, X. Chen, Y. Cheng, J. Conway, D. Cranshaw, A. Datta, A. Filenius, S. Hogan, S. Lantz, J. Monroy, H. Postema, D. Quach, J. Reichert, M. Reid, D. Riley, A. Ryd, K. Smolenski, C. Strohman, J. Thom, P. Wittich, R. Zou

Fermi National Accelerator Laboratory, Batavia, U.S.A.

A. Bakshi, D.R. Berry, K. Burkett, D. Butler, A. Canepa, G. Derylo, J. Dickinson, K.F. Di Petrillo, A. Ghosh, C. Gingu, H. Gonzalez, S. Grünendahl, L. Horyn, M. Johnson, P. Klabbers, C.M. Lei, R. Lipton, S. Los, P. Merkel, P. Murat, S. Nahn, F. Ravera, R. Rivera, L. Spiegel, L. Uplegger, E. Voirin, H.A. Weber

University of Illinois at Chicago (UIC), Chicago, U.S.A.

H. Becerril Gonzalez, S. Dittmer, A. Evdokimov, O. Evdokimov, C.E. Gerber, D.J. Hofman, C. Mills, T. Roy, S. Rudrabhatla, J. Yoo

The University of Iowa, Iowa City, U.S.A.

M. Alhusseini, S. Durgut, J. Nachtman, Y. Onel, C. Rude, C. Snyder, K. Yi[19]

Johns Hopkins University, Baltimore, U.S.A.

O. Amram, N. Eminizer, A. Gritsan, S. Kyriacou, P. Maksimovic, C. Mantilla Suarez, J. Roskes, M. Swartz, T. Vami

The University of Kansas, Lawrence, U.S.A.

J. Anguiano, A. Bean, S. Khalil, E. Schmitz, G. Wilson

Kansas State University, Manhattan, U.S.A.

A. Ivanov, T. Mitchell, A. Modak, R. Taylor

University of Mississippi, Oxford, U.S.A.

J.G. Acosta, L.M. Cremaldi, S. Oliveros, L. Perera, D. Summers

University of Nebraska-Lincoln, Lincoln, U.S.A.

K. Bloom, D.R. Claes, C. Fangmeier, F. Golf, C. Joo, I. Kravchenko, J. Siado

State University of New York at Buffalo, Buffalo, U.S.A.

I. Iashvili, A. Kharchilava, C. McLean, D. Nguyen, J. Pekkanen, S. Rappoccio

Boston University, Boston, U.S.A.

A. Albert, Z. Demiragli, D. Gastler, E. Hazen, A. Peck, J. Rohlf

Northeastern University, Boston, U.S.A.

J. Li, A. Parker, L. Skinnari

Northwestern University, Evanston, U.S.A.

K. Hahn, Y. Liu, K. Sung

The Ohio State University, Columbus, U.S.A.

B. Cardwell, B. Francis, C.S. Hill, K. Wei

University of Puerto Rico, Mayaguez, U.S.A.

S. Malik, S. Norberg, J.E. Ramirez Vargas

Purdue University, West Lafayette, U.S.A.

R. Chawla, S. Das, M. Jones, A. Jung, A. Koshy, M. Liu, G. Negro, J. Thieman

Purdue University Northwest, Hammond, U.S.A.

T. Cheng, J. Dolen, N. Parashar

Rice University, Houston, U.S.A.

K.M. Ecklund, S. Freed, A. Kumar, H. Liu, T. Nussbaum

University of Rochester, Rochester, U.S.A.

R. Demina, J. Dulemba, O. Hindrichs, S. Korjenevski

Rutgers, The State University of New Jersey, Piscataway, U.S.A.

E. Bartz, A. Gandrakotra, Y. Gershtein, E. Halkiadakis, A. Hart, A. Lath, K. Nash, M. Osherson, S. Schnetzer, R. Stone

Texas A&M University, College Station, U.S.A.

R. Eusebi

Vanderbilt University, Nashville, U.S.A.

P. D'Angelo, W. Johns

†: Deceased
1: Also at Vienna University of Technology, Vienna, Austria
2: Also at Institute for Theoretical and Experimental Physics, Moscow, Russia
3: Also at Université de Haute-Alsace, Mulhouse, France
4: Also at Institute for Data Processing and Electronics, KIT, Karlsruhe, Germany
5: Now at University of Hamburg, Hamburg, Germany
6: Now at Deutsches Elektronen-Synchrotron, Hamburg, Germany
7: Also at Horia Hulubei National Institute of Physics and Nuclear Engineering (IFIN-HH), Bucharest, Romania
8: Also at University of Cagliari, Cagliari, Italy
9: Also at Institut Polytechnique de Grenoble, Grenoble, France
10: Also at Université de Strasbourg, CNRS, IPHC UMR 7178, Strasbourg, France
11: Also at Universidad de Castilla-La-Mancha, Ciudad Real, Spain
12: Also at University of Patras, Patras, Greece
13: Also at École Polytechnique Fédérale de Lausanne, Lausanne, Switzerland
14: Also at National Technical University of Athens, Athens, Greece
15: Also at Universität Zürich, Zurich, Switzerland
16: Now at Bethel University, St. Paul, Minnesota, U.S.A.
17: Now at Karamanoglu Mehmetbey University, Karaman, Turkey
18: Now at Florida State University, Tallahassee, U.S.A.
19: Also at Nanjing Normal University, Nanjing, China